Modeling Networks and Dynamics in Complex Systems: from Nano-Composites to Opinion Formation

Feng Shi

A dissertation submitted to the faculty of the University of North Carolina at Chapel Hill in partial fulfillment of the requirements for the degree of Doctor of Philosophy in the Department of Mathematics.

Chapel Hill
2013

Approved by:

S. Shankar Bhamidi

Rick Durrett

M. Gregory Forest

Jingfang Huang

Peter J. Mucha

Abstract

FENG SHI: Modeling Networks and Dynamics in Complex Systems: from
Nano-Composites to Opinion Formation
(Under the direction of M. Gregory Forest and Peter J. Mucha)

Complex networks are ubiquitous in systems of physical, biological, social or technological origin. Components in those systems range from as large as cities in power grids, to as small as molecules in metabolic networks. Since the dawn of network science, significant attention has focused on the implications of dynamics in establishing network structure and the impact of structural properties on dynamics on those networks. The first part of the thesis follows this direction, studying the network formed by conductive nanorods in nano-materials, and focuses on the electrical response of the composite to the structure change of the network. New scaling laws for the shear-induced anisotropic percolation are introduced and a robust exponential tail of the current distribution across the network is identified. These results are relevant especially to "active" composite materials where materials are exposed to mechanical loading and strain deformations. However, in many real-world networks the evolution of the network topology is tied to the states of the vertices and vice versa. Networks that exhibit such a feedback are called adaptive or coevolutionary networks. The second part of the thesis examines two closely related variants of a simple, abstract model for coevolution of a network and the opinions of its members. As a representative model for adaptive networks, it displays the feature of self-organization of the system into a stable configuration due to the interplay between the network topology and the dynamics on the network. This simple model yields interesting dynamics and the slight change in the rewiring strategy results in qualitatively different behaviors of the system. In conclusion, the dissertation aims to develop new network models and tools which enable insights into the structure and dynamics of various systems, and seeks to advance network algorithms which provide approaches to coherently articulated questions in real-world complex systems such as social networks and composite materials.

to my beloved family

Acknowledgements

I would like to express my deep appreciation and gratitude to my advisors Dr. Mucha and Dr. Forest, for their extraordinary guidance, support and encouragement during my graduate study. I started working with Dr. Mucha almost immediately after I entered graduate school. During the past five years, I never had a single moment that I doubted this decision. It is always pleasant and rewarding to work with him. He brought me into research, into science, and into the academic world. And later he introduced me to my coadvisor Dr. Forest, who is just a great person, both scholarly and personally. In doing research, sometimes we succeeded, sometimes we failed. But every time we were challenged, they got my back and we managed to move forward. They taught me not only science, but also, more importantly, how to do science. I am very fortunate to have their mentorship.

I would also like to sincerely thank Dr. Durrett whose personality and way of doing science have a huge influence on me. It is a great pleasure working with him and every single conversation I had with him is instructive and humorous. I am also very grateful to Dr. Bhamidi for being such an important role in my graduate study—the advisor of my Master's thesis, the member of my Ph.D. committee and a friend in both life and science. And I really appreciate the valuable advice and help from Dr. Huang, whose office door was always open when I was in need of help.

To complete a project as large as a Ph.D. degree requires a network of support, and I am indebted to many people that I am not able to acknowledge here individually. I thank my professors, especially Dr. Nobel, for their valuable inputs, discussions, and accessibility. I thank my peers for making my graduate study colorful and enjoyable.

Finally, and most importantly, I would like to thank my parents. Their faith in me and their encouragement are the endless source of power to keep me moving forward.

Table of Contents

List of Figures ix

Chapter

1. Introduction 1
    1.1. Background 1
    1.2. Overview of the Dissertation 3
2. Random Resistor Networks 6
    2.1. Introduction 6
    2.2. Model and Method 9
    2.3. Results and Discussions 10
    2.4. Conclusion 20
3. Brownian Nanorod Dispersions 22
    3.1. Introduction 22
    3.2. Method and Model 25
    3.3. Results and Discussions 33
    3.4. Conclusion 45
4. Evolving Voter Model with Two Opinions 47
    4.1. Introduction 47
    4.2. Evolving Voter Model with Two Opinions 49
    4.3. Quasi-Stationary Distributions 53
    4.4. Evolution of Network Statistics 57
    4.5. Conclusion 61

5. Multi-Opinion Evolving Voter Model 63
  5.1. Introduction 63
  5.2. Multi-Opinion Model 63
  5.3. Quantitative Characterization of Quasi-Stationary Distributions 66
  5.4. Conclusion 69
References 72

List of Figures

2.1. Distribution h(x) of the logarithmic current (left panel) and distribution f(i) of the current (right panel) near threshold ($p = 0.25$) and above threshold ($p = 0.29$) in $100 \times 100 \times 100$ random resistor networks. The logarithmic transformation of currents exposes small currents which have a power law distribution (left panel) while the overall current distribution looks exponential (right panel). 11

2.2. Empirical probability density function of the current in an $L \times L \times L$ cubic lattice at bond density 0.25 (left) and at bond density 0.29 (right) for various system sizes L. The percolation threshold is at bond density 0.2488. A constant unit voltage is imposed across the system. The plot is derived from the histograms of all the currents over 1000 realizations. The inset shows the same distributions rescaled by the system L with critical exponents $u = 1$ and $v = 1$. 13

2.3. Scaling of the first 6 sample moments with respect to the system size L. The bond density is fixed at $p = 0.25$ and the system size L varies from 50 to 200. The fitted equations of the moments M_k are shown in the figure (cf. Equation (2.3)). Curves are normalized by their values at $L = 200$. 14

2.4. Limiting current distributions $f^{\infty}(i) = L^{-1} f_L(L^{-1} i)$ at different system sizes and bond densities. Colors represent the ratio $L/(p - p_c)^{-0.9}$ where $p_c \doteq 0.2488$ is the percolation threshold for an infinite system and thus the color serves as an indicator of the system size relative to the correlation length. The overlap of current distributions at different parameters demonstrates a robust exponential distribution for large currents. 15

2.5. Scaling behaviors against bond density $p - p_c^{\text{eff}}$ for the bulk conductance $C(p)$, the rate $\lambda(p)$ of the exponential tail of the current distribution, and the number $\tilde{N}(p)$ of bonds with current larger than 10^{-3}. The system size is fixed at $L = 100$ and the bond density p varies from 0.25 to 0.29. Curves are normalized by their values at $p = 0.29$. In the parent figure $p_c^{\text{eff}} = 0.24$ as defined in [1] and $p_c^{\text{eff}} = 0.2488$ in the inset. The inset demonstrates the sensitivity of the scaling exponent on the value of p_c used (with fitted exponents $1.919 \pm .012$, $1.969 \pm .077$ and $1.917 \pm .013$ respectively), but further supports the similar behavior of $\lambda(p)$ and $C(p)$. 17

2.6. Left: Scaling of the bulk conductance with respect to the bond density p in an $100 \times 100 \times 100$ cubic lattice. Right: Limiting current distributions at bond density ranging from $p = .3 - .4$. 20

3.1. An illustration of the imposed shear flow with velocity field: $\vec{v} = Pe(y, 0, 0)$, i.e., the direction of flow is along the x axis, with y axis the flow gradient direction and z the vorticity direction. 28

3.2. Plots of sample points $\boldsymbol{m}$ draw from $f(\boldsymbol{m}, t)$ viewed from top (left column) and viewed from side (right column) at 4 shear rates, from no shear (Pe=0) to strong shear (Pe=10). Each subplot contains 3000 points. 30

3.3. Left: A randomly oriented ($Pe = 0$) dispersion of aspect ratio 50 rods at volume fraction .0008. The box is four times the rod length. Right: An illustration of the network representation of a few rods. Nodes are contact points of rods (the red dots), and edges are the effective conductances between contact points (the blue lines). 31

3.4. Average number of nodes in the network (square), number of edges in the network (circle), number of edges in the percolating component (triangle), number of edges in the plate-constrained 2-core (dot), number of current-carrying edges (star) as rod volume fraction varies. All the quantities are normailized by the average number of rods. The left panel corresponds to $Pe = 0$ and the right panel corresponds to $Pe = 5$. 34

3.5. Left: The average number of edges in the rod contact network (circle), in the percolating components (triangle), in the plate-constrained 2-core (dot), and in the current-carrying paths (star), normalized by the total number of rods at each rod volume fraction. Rods are isotropically oriented ($Pe = 0$). Thus restriction to the plate-constrained 2-core filters approximately 90% of the rods near percolation threshold $\theta_c \doteq 1.3\%$, therefore reducing the problem to 10% of its original size. Right: Percolation phase diagram with anisotropic percolation thresholds in the 2-parameter space of (Pe, θ) (cf. Figure 4 in [2]). The solid, dashed and dotted curves correspond to the percolation thresholds in the x, y and z directions, respectively. 36

3.6. Scaling of the mean conductivity σ in each of the three directions against rod volume fraction $\theta - \theta_c$ for isotropic ($Pe = 0$) dispersions (left) and sheared ($Pe = 5$) dispersions (right). The power-law scaling of conductivity persists under shear, while the scaling exponent is anisotropic for $Pe > 0$. Each data point is the average of 1000 realizations in a cubic box of linear dimension 0.5 microns (10 times the nanorod length). 36

3.7. Anisotropic conductivity exponents against normalized shear rate Pe. The scaling exponents are estimated from fitting Equation 3.4 to the mean conductivity in each direction. A 95% confident interval is shown as a shaded region around each exponent. 37

3.8. Current distributions $f(i)$ (left) and logarithmic current distributions $h(x)$ (right) for isotropic ($Pe = 0$) dispersions at various rod volume fractions θ given a unit voltage source. The logarithmic transformation of currents exposes small currents which have a power law distribution (right panel) while the overall current distribution is exponential (left panel). The empirical densities are derived from the histograms of all the currents over 1000 realizations. 38

3.9. Left: Current distributions in both the flow direction (x) and the flow gradient direction (y) for sheared dispersions ($Pe = 5$). The percolation threshold is $\theta_c(x) \doteq 1.35\%$ in the flow direction (x) and $\theta_c(y) \doteq 1.4\%$ in the flow gradient direciton (y). Right: Visualization of the current-carrying rods and color-coded current values in a percolating cluster in the x direction from one realization at (Pe, θ)=(10, .015). 39

3.10. Left: current distributions in isotropic dispersions ($Pe = 0$) at rod volume fraction $\theta = 1.33\%$. Two system sizes are considered: 10 times as long as a rod ($L = 10l$) and 15 times as long as a rod ($L = 15l$). The inset shows the same distributions rescaled by the system size L with $u = 1$ and $v = 1$. Right: rescaled current distributions in the flow direction (x) and in the flow gradient direction (y) in sheared ($Pe = 5$) dispersions at rod volume fraction $\theta = 1.5\%$. It demonstrates that the finite size scaling form Equation 3.6 holds in each direction under shear. 41

3.11. Multi-scale electrical properties across the percolation phase diagram (Figure 3.5 (Right)). The top row shows the **color-coded average bulk conductivities** in the flow (x) direction (left panel), flow-gradient (y) direction (center panel), and vorticity (z) direction (right panel). The bottom row shows the **rates of the exponential current tails** in the three physical directions respectively. 44

3.12. Percolation phase diagram with anisotropic percolation thresholds in the 2-parameter space of (Pe, θ) (cf. Figure 3.5). The black solid (x), dashed (y) and dotted (z) curves correspond to the percolation thresholds in the x, y and z directions, respectively; and the red solid (v_1), dashed (v_2) and dotted (v_3) curves correspond to the percolation thresholds in the eigenvector directions v_1, v_2, and v_3, respectively. 45

4.1. Fraction ρ of voters with the minority opinion in consensus state for the rewire-to-same model (left) and the rewire-to-random model (right). Phase transitions are observed in both models as the rewiring probability α varies. Simulations start from Erdős-Rényi random graphs with $N = 100,000$ vertices and average degree $\lambda = 4$. Opinions are initially assigned randomly with the probability of opinion 1 given by $u_0 = 0.5$, 0.4, 0.3, 0.2, and 0.1. 50

4.2. Average time to consensus as the rewiring probability α varies for the rewire-to-same model (left) and the rewire-to-random model (right), showing the same behaviors for the phase transitions as in Figure 4.1. Each data point in the figure is an average over 100 simulations starting from Erdős-Rényi random graphs with $N = 10,000$ vertices and average degree $\lambda = 4$.

Opinions are initially assigned randomly with the probability of opinion 1 given by $u_0 = 0.5$, 0.4, 0.3, 0.2, and 0.1. 51

4.3. Left: Fraction ρ of voters with the minority opinion in consensus state as the rewiring probability α varies in the region near the phase transition point $\alpha_c \approx 0.43$ for the rewire-to-same model. Results for three different graph sizes $N = 5,000$, $10,000$ and $20,000$ are shown and initial fraction of the minority $u_0 = 0.5$. Right: The same plots as in the left panel rescaled by the system size. The three curves correspond to different system sizes cross at approximately $\alpha - 0.43 = 0$ (i.e., $\alpha_c = 0.43$), and they collapse for $\alpha < 0.43$. 52

4.4. Time series of the fraction $N_1(t)/N$ of vertices with opinion 1 and the fraction $N_{01}(t)/M$ of discordant edges in one simulation, starting from an Erdős-Rényi random graph with $N = 1000$ nodes and $M = 2000$ edges, and rewiring probability $\alpha = 0.3$. The initial density of ones is $u_0 \approx 0.3$. 54

4.5. Evolution of the fraction of edges that are discordant 0-1 edges, $N_{01}(t)/M$, versus the population of opinion 1 $N_1(t)/N$ when $\alpha = 0.5$ for the rewire-to-random dynamic. Five simulations starting from u=0.2, 0.35, 0.5, 0.65, and 0.8 are plotted in different colors. Each simulation starts from an Erdős-Rényi graph with N=100,000 nodes and average degree $\lambda = 4$. After initial transients, the fraction of discordant edges behaves as a function of the population of opinions. 55

4.6. Observed arches for the rewire-to-same model (left) and the rewire-to-random model (right). The specified parabolas are fits to simulation data with $N = 10,000$ nodes and average degree $\lambda = 4$. 55

4.7. Evolution of the number of oriented triples $N_{ijk}(t)/N$ versus the population with opinion 1 $N_1(t)/N$, when $\alpha = 0.5$ for the rewire-to-random model. All simulations start at $u_0 = 0.5$ because multiple runs from one starting point are enough to explore all of the arch. Each simulation starts from an Erdős-Rényi graph with N=100,000 nodes and average degree $\lambda = 4$. After an initial transient, in each subplot the observed values stay close to a curve that is well approximated by a cubic polynomial. 59

4.8. Degree distributions in the consensus state for five simulations starting at initial density of ones $u_0 = 0.1$, 0.2, 0.3, 0.4 and 0.5 respectively. The initial graphs are Erdős-Rényi random graphs with $N = 100,000$ nodes and average degree $\lambda = 4$. The probability density function of $Poisson(4)$ is shown for comparison. The rewiring probability is $\alpha = 0.6$ larger than $\alpha_c(0.1)$ but less than $\alpha_c(0.2)$. Hence the final degree distribution starting from $u_0 = 0.1$ is different from others. 60

4.9. Left: changes in the average degrees of nodes with opinion 0, nodes with opinion 1 and all the nodes in the network, against the fraction $N_0(t)/N$ of nodes with opinion 0. Simulations start from Erdős-Rényi random graphs with $N = 10,000$ nodes and average degree $\lambda = 3$. The initial density of ones $u_0 = 0.5$ and the rewiring probability $\alpha = 0.3$. Right: the number of "stubs" or edge ends in opinion i (i.e., $\sum_{\xi(v)=i} d(v)$) normalized by the total number of nodes against the fraction of 0-nodes $N_0(t)/N$. The data shown are the same as in the left panel but presented differently. 61

5.1. Top: plot of the fraction of discordant edges versus the population of opinions in barycentric coordinates for three opinions and $\alpha = 0.5$. Multiple simulations corresponding to different initial densities are shown while each one starts from an Erdős-Rényi graph with N=10,000 nodes and average degree $\lambda = 4$. Similar to the two-opinion case, the simulations quickly converge to a parabolic cap of quasi-stationary distributions. Bottom: top view of the parabolic caps of quasi-stationary distributions for α=0.1,0.2,...,0.8. The parabolic cap Eq. (5.1) are fitted to simulation data at various α's and then the level sets $E_u N_{\neq} = 0$ are plotted, which are the intersections of the parabolic caps with the $N_{\neq} = 0$ plane, as the large circles with colors indicating values of α. 65

5.2. Coefficient $c_0(\beta)$ (left) and $c_2(\beta)$ (right) in Eq. (5.1) for models with multiple opinions. Each value of the coefficients is obtained by fitting Eq. (5.1) to multiple simulations starting from Erdős-Rényi graphs with N=100,000 nodes and average degree 4. The fitting error is very small ($R^2 \approx 0.99$) except for β close to the critical values. 67

5.3. Coefficients $c_0(\beta)$ (left) and $c_2(\beta)$ (right) in Eq. (5.3) for models with multiple opinions. Each value of the coefficients is obtained by fitting Eq. (5.3) to the same data as in Figure 5.2. 68

5.4. Coefficient $c_3(\beta)$ in Eq. (5.3) for models with multiple opinions. Each value of $c_3(\beta)$ is obtained by fitting Eq. (5.3) to the same data in Figure 5.2. . . 70

5.5. Number of opinions observed at freezing for different $\beta = \alpha/(1-\alpha)$, starting from k equally likely opinions. Each data point corresponds to a simulation starting from an Erdős-Rényi graph with $100,000$ nodes and average degree 4. Results above β_k when starting from k opinions are omitted because the final density of opinions under such conditions is the same as the initial density. 70

CHAPTER 1

Introduction

1.1. Background

Complex networks are ubiquitous in systems of physical, biological, social or technological origin. Components in those systems range from as large as cities in power grids, to as small as molecules in metabolic networks. The complexity is embedded in both the heterogeneity across components and the complex (e.g., nonlinear or stochastic) interactions between them. The interdisciplinary study of such diverse systems using network tools and theories has exploded during the past two decades [3–12]. In Epidemiology, the spread of a disease is usually modeled as a contact process on networks [7, 13, 14], and clinical immunization strategies are obtained through analysis on corresponding network models [6, 15, 16]. In Biology, the neural system can be modeled as a network consisting of neurons connecting through neural fibers [4], and the main structural supports in cells are cytoskeletal polymer networks [3, 9, 17]. Perhaps the most well-known network is the Internet which is a huge network of computers and routers, and there is still controversy about whether it being a scale-free network [5, 18]. Facebook and Twitter are some of the myriad types of networks which are intimately related to our daily life. As we enjoy the convenience brought by fast information diffusion over those networks, we also suffer from the spread of undesirable information such as spam or even anti-society messages which lead to riots such as the Arab Spring in 2011. Understanding the dynamics of such networks is of great importance in practice.

Although the study of networks has a long history from graph theory (since 300 years ago) to sociology (e.g., Granovetter [19]), the emergence of network science was not seen until the first decade of the 21st century. The two seminal papers by Watts and Strogatz

[4] and Barabási and Albert [5] marked the beginning of the modern chapter of network science. It was discovered that regardless of their forms, sizes, natures, and origins, most real networks that have been observed in nature and science are driven by a common set of fundamental laws and organizing rules, which has drawn a wide class of audience to this interdisciplinary field. The interdisciplinary nature is the first feature of network science. It utilizes the conceptual framework of graph theory and probability, the tools and principles of statistical physics, the computing algorithms from computer science, and tools from statistics and other subjects to help us understand various systems in nature, society, and technology. This feature will be amplified in this thesis on the study of nanocomposites and social influences. Numerical simulations reveal interesting behaviors of the real complex systems, and abstract mathematical models such as lattice models from graph theory provide insights into those systems and help us better understand the fundamental structures. Another distinction of network science is its data-driven nature. The boom of huge datasets during the past two decades, such as the map of Internet [20], protein-protein interaction networks in human cells [21], and the human connectome [22], spurs the development of network science. This thesis focuses on the modeling aspect of networks, yet the models developed can be adapted to and compared with real data in future studies.

Since the dawn of network science, significant attention has focused on the implications of dynamics in establishing network structure, including preferential attachment, rewiring, and other mechanisms [8, 23–26]. At the same time, the impact of structural properties on dynamics on those networks has been studied intensively [27]. The first part of the thesis follows this direction, studying the network formed by conductive nanorods in nano-materials, and focuses on the electrical response of the composite to the structure change of the network. However, in many real-world networks the evolution of the network topology is tied to the states of the vertices and vice versa. Networks that exhibit such a feedback are called adaptive or coevolutionary networks [28, 29]. For instance, the status of a server changes according to the requests from established connections, and when its status reaches certain level, the server may close certain connections and result in a cascade of changes in the topology of the communication network; in opinion formation, a group of different believers might split up or become dominated by one opinion over time. Compared to the rich literature on dynamical processes on static networks, there is relatively limited study on coevolutionary networks; and simple scaling behaviors and mean field theories which succeeded previously may fail when the system dynamics and the network topology are coupled together. The second part of the thesis examines two closely related variants of a simple, abstract model for coevolution of a network and the opinions of its members.

So motivated, the dissertation focuses on the development of new network models and tools which enable insights into the structure and dynamics of various systems, and seeks to advance network algorithms which provide approaches to coherently articulated questions in real-world complex systems such as social networks and composite materials. Specifically, this thesis presents studies on current flow in random materials such as nanocomposites and opinion formation over social networks.

1.2. Overview of the Dissertation

The dissertation mainly consists of two parts (four chapters), which are based on the four papers from my interdisciplinary collaborations [30–33]. The first part (chapter 2 and 3) studies the electrical responses of nanorod composites to the resistor network formed by the rod phase. It aims to understand how the the network topology shapes the material properties. The work in both chapters has been submitted [30, 31]. The second part (chapter 4 and 5) studies the ‘evolving voter model’, an abstract mathematical model originated from opinion formation. As a representative model for adaptive networks, it displays the feature of self-organization of the system into a stable configuration due to the interplay between the network topology and the dynamics on the network. The work in chapter 4 is published in [32] and the work in chapter 5 is submitted [33].

1.2.1. Brownian Nanorod Dispersion under Shear. Different from dynamics on social networks, current flow in physical transport networks such as nano-composites obey physical conservation laws such as the set of Kirchoff's laws. The randomness of the material comes from shear-induced anisotropy of the nanorod orientation distribution due to processing history. The goal of this collaboration (including Dr. Zheng from Kent State University, Dr. Zhou from Old Dominion University, Simi Wang and my advisors Dr. Forest and Dr. Mucha) is to develop understandings of multi-scale (local and bulk) electrical properties respective of the statistical mechanics and anisotropy of the material.

Our study of the physical nanorod system starts with the random resistor network which is a random lattice in which each edge is present with probability p and takes unit conductance if present. By large scale simulations and finite size scaling analysis we identify an universal exponential distribution of large currents [30]. This work is included in chapter 2.

Our numerical algorithm for a shear nanorod dispersion consists of three steps. The first step is to compute the distribution of the rod orientation by numerically solving the Doi-Hess-Smoluchowski equation of rigid-rod liquid crystalline polymer kinetic theory. The second step uses the resulting distribution to populate Monte Carlo samples of 3D sheared nanorod dispersions. In the third step, every ensemble of nanorods is mapped to a resistor network which then can be simplified using network tools. Finally the Kirchoff's equation is solved to obtain currents in the network. Using this tool we find new scaling laws for the shear-induced anisotropic percolation and a robust exponential tail of the current distribution [31]. This work is included in chapter 3.

1.2.2. Opinion Formation: the Evolving Voter Model. Inspired by Holme and Newman [34], we (including Dr. Durrett and Dr. Sivakoff from Duke Math, Dr. Gleeson from Limerick Math, Dr. Lloyd from NCSU Math, Dr. Socolar and Chris Varghese from Duke Physics, and Dr. Mucha) study a simple yet representative example for coevolutionary networks, the evolving voter model. Although it is called a voter model, we not only tend to answer questions in opinion formation, but also target at the development of fundamental models and theories for adaptive complex systems.

Starting from a random graph with each node assigned randomly an opinion from k possible opinions, at rate 1 we pick an edge uniformly at random. If the two endpoints of the edge have different opinions, two events may occur: rewiring and voting. With probability α the edge breaks up and one node of the two will link to someone else in the network (rewiring), and with probability $1 - \alpha$ one of the two will adopt the other's opinion (voting). The system will finally enter a consensus state in which every pair of connected nodes has the same opinion.

We have studied the simplest case of this model in [32] in which there are only two possible opinions and two rewiring strategies. This simple model yields interesting dynamics and the slight change in the rewiring strategy results in qualitatively different behaviors of the system. This work is included in chapter 4. In our most recent work [33] we extend this model to the one with infinitely many opinions. The quasi-stationary distribution of opinions is found to persist in higher dimensions and there are infinitely many phase transitions. This work is included in chapter 5.

CHAPTER 2

Random Resistor Networks

2.1. Introduction

Random resistor networks are intimately related to bond percolation which dates back to Broadbent and Hammersley [35]. As a well studied subject in percolation theory, bond percolation was first introduced as a model for diffusion through porous medium, e.g., water penetrating a porous solid [35]. Different from conventional diffusion, the medium is highly heterogenous and even random, hence demanding different treatments. The mathematical representation of such a system is a d-dimensional integer lattice $\mathbb{Z}^d$. Let $d(x, y)$ be the graph distance between two lattice points $x = (x_1, ..., x_d)$ and $y = (y_1, ..., y_d)$, i.e., $d(x, y) = \sum_{i=1}^{d} |y_i - x_i|$. The lattice $\mathbb{Z}^d$ can be turned into a graph by connecting all pairs of points x and y if $d(x, y) = 1$. For bond percolation, each edge in the graph is open for "fluid" to pass with probability p, and closed with probability $1 - p$. The open edges are called bonds by convention and hence this process is called bond percolation.

A variation of bond percolation is called site percolation in which each lattice point is open (for fluid to pass) with probability p and closed with probability $1 - p$, and only edges between two open neighboring lattice points are present. This version is usually used to model the transmission of "diseases". For example, in a hypothetical forest where trees are grown on a square lattice, a healthy tree may be infected by a neighboring blighted tree with probability p. Besides, there is a large array of variations such as the combination of the above two processes (site-bond percolation), and same processes as the above but on different lattices.

Despite so many types of percolation, the first question studied in percolation theory is that when there will be a percolating path (i.e., a path of open edges and/or nodes) connecting the two opposite ends of a finite lattice. In other words, for a given p, what is the probability of having a percolating path from one side of the lattice to the other? This seemingly easy question is actually hard, and things become simpler on an infinite lattice. For an infinite system there is a critical p, called percolation threshold p_c. Below p_c all the clusters (of nodes connected by open edges) are small and the probability that an infinite cluster exists is zero; above p_c an infinite cluster emerges and the probability of having an infinite cluster is one. That is to say, there is always an infinitely long percolating path above p_c. The critical point p_c is a singularity and theoretical results at p_c is limited to certain special lattices. Even there is not a theoretical prediction for the value of p_c in general. (It took 20 years to prove that $p_c = 1/2$ for bond percolation on the 2D quare lattice $\mathbb{Z}^2$ [36].) For most lattices the percolation thresholds cannot be calculated analytically, and a significant amount of work is devoted to estimating them numerically [37].

Besides percolation thresholds, percolation theory has studied various topological properties of the models, e.g., distribution of cluster sizes, correlation length, etc. Research on dynamical properties (i.e., properties induced by dynamical processes) such as electrical or thermal conductivity is more recent but growing rapidly because of applications in a broad range of topics in materials science, epidemiology, geology, etc. The area is too broad for this thesis to be exhaustive; the present work contributes to the understanding of current distributions in random resistor networks, which lays the foundation for further study on nanorod dispersions. Previous results related to this work will be briefly recalled when necessary and interested readers can refer to [36, 38–40].

Motivated by questions about macroscopic electrical properties in materials science, this chapter revisits the classical problem of bond percolation [38, 39] in a three-dimensional $L \times L \times L$ cubic lattice and the scaling of the currents conducting through the percolating bonds. In the seminal work of de Arcangelis *et al.* [41, 42], a hierarchical lattice model is given for the percolating backbone of the network, which yields a log-normal current distribution in the network; this model was later generalized by Lin *et al.* [43]. These models successfully capture the multifractal behavior of the current distribution at percolation threshold (e.g., an infinite hierarchy of exponents in the moments). However, they fail to predict the power law distribution of small currents (Straley [44] and Duering *et al.* [45, 46]), and they do not address additional features of the current distribution that are most relevant to materials applications (specifically, the large current distribution properties).

Current distributions and their scaling behavior have fundamental importance in materials science. Low moments of the current distribution dictate physically measurable properties, e.g., the second moment describes the bulk conductance [41, 47]. Therefore, measurable macroscopic scaling behavior at or above percolation threshold (cf. [48]) is inherited from the current distribution. Another illustration is in the study of breakdown of random media [49–52]. This critical network property motivated studies on the size and location of the largest current in the network [53–56]. Li and Duxbury [54] showed that the logarithmic scaling of the largest current with respect to the system size is consistent with an exponential tail of the current distribution. Chan *et al.* [53] showed that large currents in a "funnel-shaped" region had an exponential distribution. Note that the maximum current does not fully characterize the large current tail of the distribution, which dominates material properties.

This chapter analyzes the entire current distribution, reproducing the power-law distributions of small currents [44–46] while revealing the dominating extent of an exponential large current tail. It then takes moments to show the robustness of the exponential large current tail above criticality which is independent of the bond density given a unit uniform electric field in the system. Lastly it shows how the exponential current tail controls macroscopic properties such as the scaling behavior of the largest current and the power-law scaling of the bulk conductivity.

2.2. Model and Method

A random resistor network is an $L \times L \times L$ cubic integer lattice in which each edge of the lattice takes conductance 1 with probability p (it is traditional to call such a conducting edge a bond and p is the bond density), and conductance 0 with probability $1 - p$. The goal is to understand the relationship between the electrical and topological properties of the resulting bond percolation network. In order to model an externally-driven bulk electrical response, two perfectly conducting $L \times L$ plates are considered to be present at opposite ends of the cube, representing the sink and source of current (in response to either an external voltage drop or current source).

The bond percolation threshold p_c for an infinite 3D cubic lattice is $p_c \doteq 0.2488$ [57]. For $p < p_c$, all clusters are small and almost surely no percolating cluster forms in an infinite network. Above p_c an infinite cluster emerges with probability one that spans the network, i.e., the network has a percolating cluster. There is a significant literature devoted to the scaling behavior of the distribution of cluster sizes. The typical representation is in terms of a power law with a exponential cutoff [39],

$$n_s \propto s^{-\tau} \exp(-|p - p_c|^{1/\sigma} s),$$

where n_s is the number of clusters with s bonds. Nonetheless, there is no known connection between the cluster distribution scaling and the distribution of currents supported on the cluster distribution. Indeed, the non-zero values of the current distribution are associated with the geometric properties of only those clusters that percolate, whereas all other clusters are lumped together in the zero current value. Clearly, some connection exists between this cluster size scaling and the small and large tails of the current distribution, yet this remains an open problem.

With this background, the simulation procedure is now summarized. The physical distribution of currents is solved by large-scale simulations of the random resistor network. Specifically, for each realized graph of the random resistor network model in which nodes correspond to the lattice points and edges to the conducting bonds, a breadth-first search algorithm [58] identifies the union of percolating clusters that connect the two plates. The key ingredient is the plate-constrained 2-core — defined here as the connected subgraph containing both boundary plates with degree at least two in the interior of the subgraph. *This plate-constrained 2-core captures all bonds that potentially carry non-zero current in the posed problem.* This pre-processing step provides two significant advantages. 1. Restriction to the plate-constrained 2-core filters approximately 90% of the bonds near percolation threshold, therefore reducing the linear system to 10% of its original size. 2. By *a priori* elimination of all bonds not in the plate-constrained 2-core, a vast fraction of exactly zero-current bonds are removed from the numerical simulation of the linear system, thereby improving numerical precision overall, and in particular improved resolution of the small current tail. Kirchhoff's law [59] is then solved on the plate-constrained 2-cores with a standard linear solver, giving the current on each bond. A statistical description of the network properties is obtained by averaging over 1000 realizations for each bond density and system size.

2.3. Results and Discussions

2.3.1. Multiscale Current Distributions. Because it is extremely rare that a bond in the percolating backbone carries exactly zero current, bonds according to zero current (within numerical precision) are separated from all the rest, and only the non-zero currents are analyzed. Let $f(i)$ denote the probability density function (PDF) of the currents across the population of current-carrying bonds (that is, ignoring zero-current bonds where present). Let $h(x)$ be the corresponding PDF (again, restricted to non-zero currents) of the logarithmic current $X = \ln(I)$. The two distributions are related by $h(x) = f(e^x)e^x$.

The logarithmic current distribution $h(x)$ and current distribution $f(i)$ near ($p = 0.25$) and above ($p = 0.29$) the threshold are shown in Figure 2.1 *for a unit voltage source.* (The alternative formulation of a unit current source is considered in 2.3.3.) First, the logarithmic transformation of current exposes the small current region; the

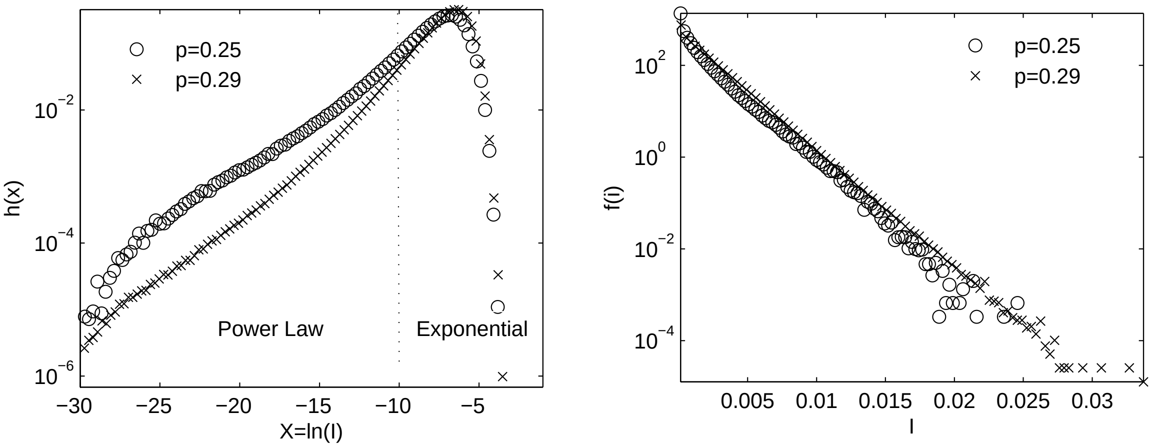

Figure 2.1. Distribution h(x) of the logarithmic current (left panel) and distribution f(i) of the current (right panel) near threshold ($p = 0.25$) and above threshold ($p = 0.29$) in $100 \times 100 \times 100$ random resistor networks. The logarithmic transformation of currents exposes small currents which have a power law distribution (left panel) while the overall current distribution looks exponential (right panel).

left panel in Figure 2.1 recapitulates the small currents [44–46]. Second, for relatively large currents (i.e., to the right of the peak of the $h(x)$ distribution), Figure 2.1 (right) is clearly suggestive of exponential current distributions. This general shape of the current distribution persists as bond density p increases above threshold for a "distance" $p - p_c$ to be clarified below relative to persistence of the small current scaling. The implications are two-fold: an exponential large current tail at percolation that persists for $p - p_c$ at finite non-zero values; a small current tail that disintegrates relatively rapidly above the critical bond density. Scattering can be observed in the current distribution at $p = 0.25$ because of finite size effects since the $p = 0.25$ correlation length [39] is larger than the system size $L = 100$. Specifically, near threshold, the correlation length ξ scales as $\xi \propto (p - p_c)^{-0.9}$ [39], a feature that we will incorporate in our study below.

While the small-current behavior is well understood and the maximum current has been studied extensively, little is known or has been reported about the large current tail of the distribution — even though the large currents dominate bulk properties. This is not so surprising in retrospect. The theoretical allure of the physics community has focused primarily on universality of power law scaling at percolation threshold, which is revealed by the small current tail as one approaches criticality from above. On the other hand, concerns of network failure draw attention to the largest current in the network. The bridge between these scaling behaviors (i.e., the large current tail), and the relative robustness of both tails of the distribution above percolation, do not appear to be addressed in the literature (with the caveat noted earlier of a cut-off function in analysis of the cluster size distribution).

2.3.2. Finite Size Scaling Analysis. This subsection focuses on the large current tail, revealing a robust exponential distribution above and close to percolation threshold, yet persistent farther from threshold than the small current power law scaling. The empirical densities of the current for a unit voltage source near percolation threshold ($p = 0.25$) and above threshold ($p = 0.29$) for different system sizes are shown in Figure 2.2. Despite slightly larger noise at bond density $p = 0.25$, the straight lines at both bond densities point to exponential tails of the current distributions, and the rate of the exponential decay increases with the system size L. In order to meaningfully capture an externally-imposed voltage drop in the thermodynamic limit ($L \to \infty$), and to better understand the effect of system size on the current distribution, a finite-size scaling analysis is carried out on the distributions. Let $f_L(i)$ be the probability density function (PDF) of the current at system size L for a unit voltage source; then by properly rescaling $f_L(i)$ with L, the effect of the system size is eliminated:

$$L^{-u} f_L(L^{-v} i) = f^{\infty}(i), \tag{2.1}$$

where $f^{\infty}(i)$ is a function independent of L, and u and v are unknown exponents to be determined. By tuning u and v, the densities for different system sizes collapse onto a single curve with $u = 1$ and $v = 1$ (see the insets of Figure 2.2). This is the expected result for a material with bulk conductance: the total resistance of the cube per unit cross-sectional area increases $\sim L$. This results in $v = 1$, while $u = 1$ yields the correct normalization factor so that the rescaled PDF integrates to 1. In other words, $f^{\infty}(i)$ is the limiting current distribution for system size L and external voltage source $V^* = L$

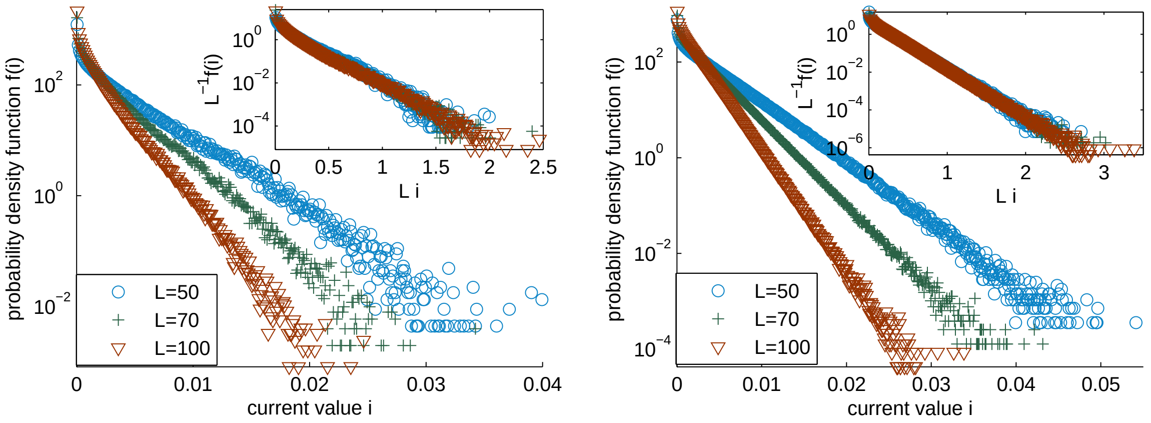

FIGURE 2.2. Empirical probability density function of the current in an $L \times L \times L$ cubic lattice at bond density 0.25 (left) and at bond density 0.29 (right) for various system sizes L. The percolation threshold is at bond density 0.2488. A constant unit voltage is imposed across the system. The plot is derived from the histograms of all the currents over 1000 realizations. The inset shows the same distributions rescaled by the system L with critical exponents $u = 1$ and $v = 1$.

(i.e., a unit uniform electric field, up to edge effects). Therefore in a finite system the current density for a unit voltage source scales as:

$$f_L(i) = L\, f^{\infty}(Li). \tag{2.2}$$

It might seem natural that the current distribution will not change with system size L if the electric field in the system is kept constant as L increases. However, the simple scaling form in equation (2.2) is not trivial. It implies that the multifractal property of the current distribution [42] comes from small currents, since the large current tail has a simple scaling form with respect to the system size. Specifically, the k^{th} moment M_k of the large currents described by this finite-size scaling is a simple scaling function of L:

$$M_k = \int_0^{\infty} i^k f_L(i)\, di = \int_0^{\infty} i^k L\, f^{\infty}(Li)\, di \propto L^{-k}. \tag{2.3}$$

To confirm this simple scaling form of the moments, the first several sample moments at bond density 0.25 are computed for varying system sizes and plotted in Figure 2.3.

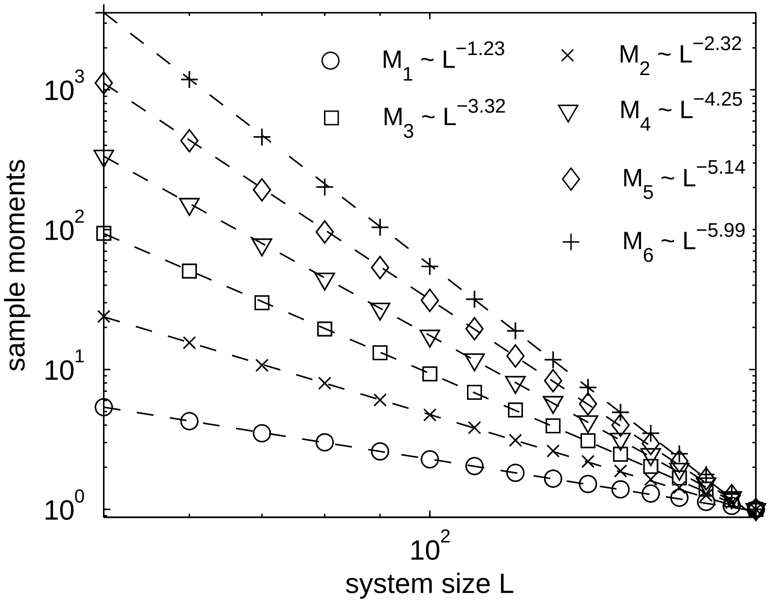

FIGURE 2.3. Scaling of the first 6 sample moments with respect to the system size L. The bond density is fixed at $p = 0.25$ and the system size L varies from 50 to 200. The fitted equations of the moments M_k are shown in the figure (cf. Equation (2.3)). Curves are normalized by their values at $L = 200$.

The sample moments are calculated as $\hat{M}_k = \frac{1}{N}\sum_b i_b^k$, where N is the number of bonds with nonzero current and the sum of bond currents i_b is taken over all current-carrying bonds, b. The scaling forms of the moments are not exactly the same as Equation (2.3) due to the multifractal property of small currents and numerical error; however for large moments the exponential tail of the current distribution becomes dominant and thus the scaling relationship approaches Equation (2.3).

2.3.3. Robustness of the Exponential Current Tail above Criticality. Given the simple scaling form of the large current distribution with respect to system size, this subsection examines the robustness of the exponential tail of the current distribution above criticality and its scaling with bond density p. The limiting current distributions $f^{\infty}(i) = L^{-1}f_L(L^{-1}i)$ for a wide range of system sizes L and bond densities p are superimposed on each other in Figure 2.4, with colors representing the ratio $L/(p - p_c)^{-0.9}$ as an indicator of the extent to which our result is affected by the finite size effect. Large

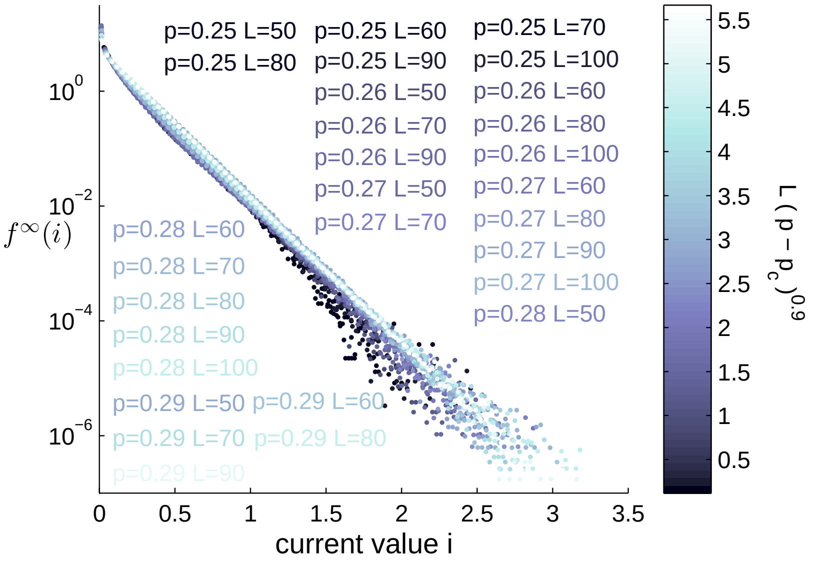

FIGURE 2.4. Limiting current distributions $f^\infty(i) = L^{-1}f_L(L^{-1}i)$ at different system sizes and bond densities. Colors represent the ratio $L/(p-p_c)^{-0.9}$ where $p_c \doteq 0.2488$ is the percolation threshold for an infinite system and thus the color serves as an indicator of the system size relative to the correlation length. The overlap of current distributions at different parameters demonstrates a robust exponential distribution for large currents.

values of this ratio indicate that the system size is larger than the correlation length and hence there limited finite size effect exists. Despite the noise at low system-size-to-correlation-length ratios, *Figure 2.4 demonstrates apparent convergence to a robust class of exponential distributions for the large current tails both near and above threshold. The rate of the exponential tail does not depend on the bond density and the simple scaling form of the tail of the distribution with respect to the system size remains the same.* Note that this robust feature of current distributions only holds sufficiently close to threshold. For instance, at saturation ($p = 1$) the current distribution approaches a delta function which is the current distribution at $p = 1$ where every bond on the straight-line paths perpendicular to the two plates carries the same current while all other bonds carry zero current.

To quantitatively confirm the independence of the exponential tail on the bond density p given a unit voltage source, a unit current source flowing between the two plates is considered. Current distributions for a unit voltage source differ from those for a unit current source by a factor of the bulk conductance C, because of the linearity of the system. Formally, denoting the density of the current distribution for the unit current source by $g_L(i)$, the density $f_L(i)$ of the current distribution for a unit voltage source can be written as: $f_L(i) = g_L(i/C)/C$. Then assuming $g_L(i) \sim e^{-\lambda(p)i}$ for large currents yields

$$f_L(i) \sim \exp\{-\frac{\lambda(p)}{C(p)}i\}. \tag{2.4}$$

Therefore, the rate of the exponential tail of $f_L(i)$ being independent of the bond density (over an observed range) indicates a linear relationship between the rate $\lambda(p)$ of decay of the exponential tail of $g_L(i)$ and the bulk conductance $C(p)$, and vice versa.

It would seem surprising for these two properties to scale linearly with one another. To quantify this relationship, exponential distributions are fitted to the current distributions for a unit current source at various bond densities and their rates $\lambda(p)$ are plotted against the bond densities p in Figure 2.5, along with the scaling behavior of the bulk conductance $C(p)$. To account for the finite size effect in our system, the scaling behaviors are analyzed with respect to $p - p_c^{\text{eff}}(L)$ where $p_c^{\text{eff}}(L)$ is defined as the effective percolation threshold for a finite system in Stauffer *et al.* [1]. Figure 2.5 demonstrates that the quantitative details of these power-law scalings are sensitive to the choice of $p_c^{\text{eff}}(L)$, yet the point of emphasis here is that for either choice taken, there is a persistent linear relationship between the rate of exponential decay $\lambda(p)$ and the bulk conductance $C(p)$. These results indicate that $\lambda(p)$ and $C(p)$ have similar scaling behaviors with respect to bond density near and above the percolation threshold.

Again, both the underlying exponential distribution and the power-law scalings break down far above threshold, e.g., when $p \geq 0.35$.

2.3.4. Scaling Behaviors of the Largest Current. Given the explicit exponential form of the tail of the current distribution, it is easy to calculate the statistics of the largest current in the system and the result shows that they scale logarithmically with

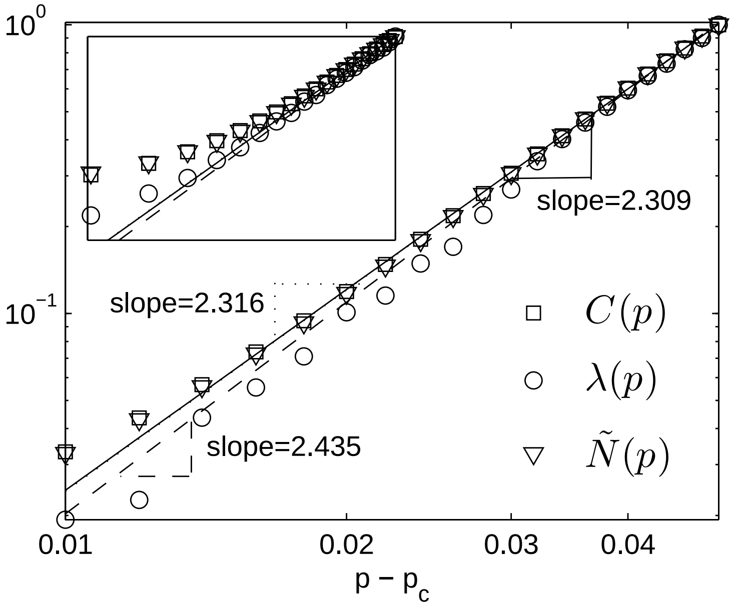

FIGURE 2.5. Scaling behaviors against bond density $p - p_c^{\mathrm{eff}}$ for the bulk conductance $C(p)$, the rate $\lambda(p)$ of the exponential tail of the current distribution, and the number $\tilde{N}(p)$ of bonds with current larger than 10^{-3}. The system size is fixed at $L = 100$ and the bond density p varies from 0.25 to 0.29. Curves are normalized by their values at $p = 0.29$. In the parent figure $p_c^{\mathrm{eff}} = 0.24$ as defined in [1] and $p_c^{\mathrm{eff}} = 0.2488$ in the inset. The inset demonstrates the sensitivity of the scaling exponent on the value of p_c used (with fitted exponents $1.919 \pm .012$, $1.969 \pm .077$ and $1.917 \pm .013$ respectively), but further supports the similar behavior of $\lambda(p)$ and $C(p)$.

respect to system size L, agreeing with the literature [53–56]. Let M_n be the largest current in the network with n bonds and $F_{M_n}(i)$ be the cumulative distribution of M_n. Then assuming weak dependence between bonds and an exponential tail of the current distribution $f_L(i) \sim \exp(-i)$, $F_M(i)$ can be expressed asymptotically as

$$F_{M_n}(i) \sim (1 - e^{-i})^n \tag{2.5}$$

for large current i. Therefore the mean of M_n is

$$\begin{aligned} \langle M_n \rangle &\approx \int_0^\infty i \cdot n(1 - e^{-i})^{n-1} e^{-i} di \\ &= \sum_{\mu=1}^{n} 1/\mu \sim \ln n + \gamma. \end{aligned}$$

Substituting in $n = pL^3$, the logarithmic scaling of the mean largest current $\langle M_n \rangle \sim \ln L$ is recovered. Similarly, solving $F''_{M_n}(i) = 0$ confirms that the mode of M_n is also $\ln n$, and the characteristic largest value [60], which is the $(n-1)^{\text{th}}$ n-quantile of the current distribution, is calculated to be $\ln n$ as well. Note that the scaling of the largest value of a distribution does not generally imply the shape of the distribution, since it is not hard to construct different distributions with the same largest current scaling behavior. However, the current distribution in this model results from a regular physical system and hence it is expected to have a regular tail. Li *et al.* [54] showed that the logarithmic scaling of characteristic largest value would imply an exponential tail of the current distribution. The present work has not only identified an exponential tail but, more strongly, has demonstrated that this exponential behavior dominates the current distribution and the resulting macroscopic properties. Moreover, the dependence of that exponential on bond densities in a range above the percolation threshold is identified.

2.3.5. Large Current Tail and Scaling of the Bulk Conductance. Recall that the second moment of the current distribution is related to the conductance of the network. This subsection connects the above scaling results for the current distribution to the experimentally reported power-law scaling of the macroscopic conductance [48]. The aim is to show that the scaling behavior of bulk conductance is inherited from the scaling of the current distribution, and in particular, it is inherited from the large current tail. Specifically, conservation of the energy in the system gives,

$$\frac{V^2}{R} = \sum_b i_b^2 r_b, \tag{2.6}$$

where V and R are the external voltage and the bulk resistance of the system respectively, i_b is the value of the current on a bond, $r_b = 1$ is the resistance of a bond, and the sum is taken over all bonds with nonzero current. For a unit external voltage source, Equation (2.6) can be rewritten as $C = R^{-1} = \sum_b i_b^2$, where C is the bulk conductance of the network. Dividing by the number of current-carrying bonds N, the conductance is recovered from the continuous current distribution:

$$\frac{C}{N} = \frac{\sum i_b^2}{N} = \int_0^\infty i^2 f_L(i)\, di. \tag{2.7}$$

Equation (2.7) connects the scaling behavior of the bulk conductance to that of the current distribution. Since the second moment of the current distribution $f_L(i)$ is dominated by the exponential tail of $f_L(i)$ which is shown to be independent of the bond density p, the number $\tilde{N}(p)$ of bonds carrying large currents (whose magnitudes are assumed to be larger than 10^{-3}) and the bulk conductance $C(p)$ have the same scaling form with respect to the bond density p, as demonstrated in Figure 2.5. *The balance of Equation (2.7) conditioned on large currents reveals an intrinsic consistency between the power-law scaling of the conductance and the exponential large current tail of the current distribution.*

2.3.6. Scaling Behaviors Far from Threshold. Near and above threshold $p_c \doteq 0.2488$ various macroscopic electrical properties such as the bulk conductance and the number of bonds with large current have power-law scaling behaviors as shown above, and there exists a robust and universal exponential distribution describing large currents. Note that both the power-law scalings and the underlying exponential distributions become invalid further from the threshold as the system saturates.

Figure 2.6 (left) plots the bulk conductance for bond densities up to 0.5. The bulk conductance gradually deviates from the power-law scaling near threshold after $p = 0.3$. Figure 2.6 (right) shows the current distributions at large bond densities with colors representing the bond density p, where p ranges from 0.3 to 0.4. The current distribution at $p = 0.3$ still agrees with the universal exponential distribution while as p increases it approaches a delta function which is the current distribution at $p = 1$ where every bond on the paths perpendicular to the two plates carries the same current while all other bonds carry zero current.

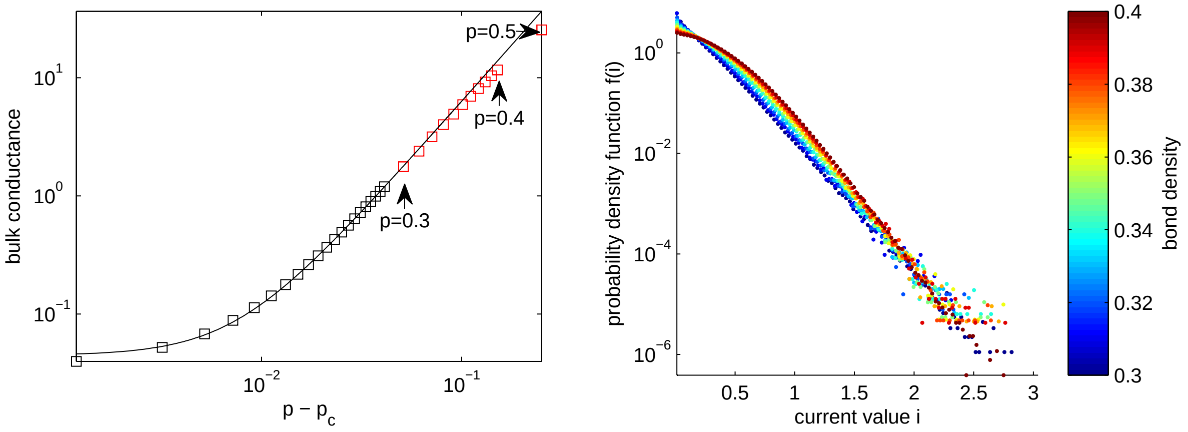

FIGURE 2.6. Left: Scaling of the bulk conductance with respect to the bond density p in an $100 \times 100 \times 100$ cubic lattice. Right: Limiting current distributions at bond density ranging from $p = .3 - .4$.

2.4. Conclusion

The present chapter has identified a robust exponential large current tail of the global current distribution in 3D random resistor networks for the boundary value problem of conductance between two infinite parallel plates. This feature persists above percolation threshold at bond densities for which the celebrated small current power law scaling has already disintegrated. In the supercritical regime above percolation threshold, it is precisely this range of currents that is most relevant for describing and diagnosing the macroscopic electrical response for materials applications. The numerical simulations leverage a network graph representation, whereby a breadth-first search preconditioner removes a large fraction ($\sim 90\%$) of the *a priori* zero current carrying bonds. This approach both reduces the linear system to allow larger system sizes at fixed computational cost, and gives significantly better accuracy for capturing scaling behavior of the small current tail.

There is possibly a geometric scaling behavior in the percolating bond component that underlies this exponential large current tail, yet this remains an open question. Finally, this property of the large current tail appears not to have been addressed in the literature previously that can be ascertain. The exponential cut-off in the cluster size distribution may very well be related, as suggested by Dr. Michael Rubinstein at one of my talks.

CHAPTER 3

Brownian Nanorod Dispersions

3.1. Introduction

Nanorod (rods with nm-scale diameters and large aspect ratio) dispersions in poorly conducting matrices possess remarkable macroscopic property enhancements when there is percolation in the rod phase. Analogous mechanical property enhancements are observed in nanorod-reinforced materials [48] and furthermore in diverse biological materials including spider silk and many instances of fibrillar protein assemblies (see Veerman *et al.* [61] and references therein). While transport properties at percolation threshold are well understood [39, 40], we are interested in sheared thin films of nanorod dispersions with two additional features of materials engineering relevance: volume fractions above percolation threshold for property stability, and anisotropy in the particle phase due to processing history [62–64] that is inherited by all properties concentrated on the particle phase. Each of these features moves anisotropic nanorod composite films out of the universality class of equilibrium percolation theory. Given the extensive literature on rod ensembles with isotropic or assumed anisotropic equilibrium orientational distributions [65–71], we are interested in how the threshold scaling behavior, widely used for guidance in materials engineering, is either perturbed or potentially strongly modified for sheared nanorod composites.

Unlike sheared carbon nanotube dispersions [62, 64, 72], nanorod orientational distributions are governed by rod rotational Brownian motion and nonlocal excluded volume interactions coupled to shear flow. Thus one should evaluate properties on the basis of statistical distribution functions of the rod ensemble, which the authors [73, 74] have previously studied in detail from the kinetic theory of Doi [75] and Hess [76]. Homogenization theory [77–79] (based on volume and ensemble averaging of kinetic distribution functions) yields accurate, anisotropic bulk conductivity tensors in sheared nanorod dispersions *below percolation thresholds*, where the scaling is linear in rod volume fraction, but fails to account for percolation in the rod phase and thereby misses the dramatic power law scaling in conductivity enhancements at and above percolation threshold. Our goal here is to extend the homogenization results [77–79] below threshold to above threshold, again relying on pre-computed kinetic orientational distributions of sheared nanorod dispersions, yet introducing new methods focused on percolation in the rod ensemble. We also note that boundary confinement in thin films can generate significant spatial gradients in the nanorod orientational distribution [80–82], yet in this work we focus first at the cubic micron scale where spatial homogeneity can be safely assumed (the so-called monodomain scale).

An additional consequence of nanometer scale particle composites is that relatively little is known about performance properties *within* the particle phase due to a lack of experimental resolution at scales bridging single nanorods to the bulk. We focus on current distributions within the particle phase in this article, highlighting multi-resolution, statistical tools to circumvent the lack of measurements. Previous predictions of current distributions, and in particular the small current tails and the scaling of the largest current in the network, have been limited to lattice resistor networks [30, 41, 44–46, 53]. The lack of progress on multi-scale transport properties in physical nanorod dispersions may be attributed both to the lack of sufficient experimental results on local properties and to the notion that lattice percolation and continuum percolation belong to the same universality class. In any case, the non-equilibrium and highly anisotropic features of sheared nanorod dispersions violate assumptions of classical percolation theory at criticality. Classical percolation theory explains the critical bulk threshold behavior in model systems, but very little is known about the property implications of several features studied herein: the scaling behavior above threshold (does it return to linear scaling with volume fraction?); the influence of shear processing (anisotropy of the particle phase); multi-scale features of the current carrying rods (e.g., the fraction of rods with non-zero current, the spatial morphology of the current carrying rods); and, the distribution of currents (especially the large current tail) supported by the nanorod ensemble.

So motivated, we develop multiscale electrical property metrics based on percolation in the particle phase that are reflective of the statistical properties and anisotropy of sheared Brownian nanorod dispersions. We focus on material systems with three distinctive properties: the nanorods are highly conducting relative to the matrix (cf. [48, 83, 84]); the rod orientation distribution may be weakly or strongly anisotropic, induced by shear flow [85, 86]; and the rod phase has macroscopic percolating clusters [2]. The first property can be relaxed with a significant increase in computational complexity of the linear electrical property transport solve. The latter two properties, however, distinguish nanoscale rod composites for which existing property assessments are inadequate for realistic particle number densities and the number of realizations required for reasonable statistics, even at fixed rod volume fraction and Peclet number (Pe, shear rate normalized by rotational relaxation rate of the Brownian rods). Buxton and Balazs [87] are quite close in spirit to our work, whereas their model focuses on polymer-nanorod surface chemical interactions and our approach is amenable to hydrodynamics of nanorod dispersions. We also utilize a network representation and graph algorithms to significantly reduce the transport property solve, and indeed to remove numerical error in the small current tail of the current distribution across the network. Similar network-based methods with fewer rod particles are used in the study of dielectric properties [88] and topology of the composite [89] by Simoes, Vaia and collaborators, which motivated our approach.

We outline our method as a series of steps in section 3.2, referring to original publications for details of our previous results that are employed here. Then we go into detail in section 3.2.3 for the new steps involving property metrics based on the network representation of percolating components. The details for numerical simulations including the values of parameters are summarized in section 3.3, followed by results on the bulk conductivities and current distributions across the percolation phase diagram.

3.2. Method and Model

3.2.1. Method. Here we study Brownian nanorod dispersions where contact percolation occurs well below the nematic transition (see [2], for example). Externally imposed shear induces anisotropic rod orientations which are reflected in the local and bulk properties carried by anisotropic percolating paths. Modeling single-particle electrical response by effective resistance proportional to path length, we statistically assess multi-resolution (local and bulk) electrical properties of a highly conducting rod particle phase dispersed in a relatively very poorly conducting matrix phase.

Our first step is to calculate the rod orientational probability distribution function (PDF) of a sheared nanorod dispersion by numerically solving the Doi-Hess-Smoluchowski equation which takes into account the effects of Brownian motion and particle-particle interactions. We refer to Forest *et al.* [74] for the kinetic theory and attractor phase diagrams of the nanorod orientational distributions versus rod volume fraction θ and normalized shear rate or Peclet number Pe. These orientational distributions arise from imposed simple shear with a presumed rapid quench of rod microstructure. For each θ and Pe we compute the kinetic distribution function, thereby creating a database of distributions across the (Pe, θ) parameter space. (Since it turns out that percolation in the rod phase occurs at volume fractions well below the nematic transition, we focus this study at volume fractions where the unsheared stable equilibrium is isotropic [2]).

The second step populates Monte Carlo (MC) samples of 3D sheared nanorod dispersions in a cubic box of length L at each fixed (Pe, θ), as in Zheng *et al.* [2]. The nanorods are randomly distributed in space with the orientation of each rod independently drawn from the corresponding orientational distribution. The rods are modeled as cylinders of length l and diameter d with two spherical caps, representing monodisperse soft-core spheroids. Since we do not check for overlap between particles in this step, the Balberg formula [66] is adopted to determine the number N of rods for a given rod volume fraction θ:

$$N = \frac{\ln(1-\theta)^{-1} L^3}{V}, \tag{3.1}$$

where V is the volume of a single rod. For rods that are partially out of the box, periodic boundary conditions are applied so that the correct rod volume fraction is achieved.

In the third step, we extend the algorithm in Zheng *et al.* [2] to identify the percolating network across a specified dimension of the simulated sample; we do so by introducing a network representation of the rod ensemble and utilizing network algorithms to identify and restrict to the percolating paths (as described below). One can solve the whole resistor network problem by any standard solver such as SPICE [71]. However, our *a priori* elimination filters many zero-current rods; there may be "dangling" clusters connected to the percolating paths that are not filtered here as we pragmatically balance computational impacts, as further demonstrated below. We then solve the corresponding resistor network problem, restricted to the percolating components, which significantly reduces the size of the system and improves numerical precision especially in the highly sensitive small current tail of the current distribution. These steps are carried out for many Monte Carlo (MC) realizations at each point across the (Pe, θ) phase diagram, generating a database of electrical properties superimposed onto the dimensional percolation phase diagram (as we will see in the results below in Figure 3.5 (Right)). We then perform statistical analysis of this database that describes electrical properties in several ways, including visual depictions.

3.2.2. Orientation of Nanorods under Shear.

Before introducing the network representation, this subsection digresses into fluid dynamics—orientation of rods under shear—to provide necessary backgrounds of the model used here for the nanorod orientations, which distinguishes sheared nanorod dispersions from previous study on rod systems. The motion of ellipsoidal particles immersed in fluid flow is a long-studied area of fluid dynamics. Following Jeffery's seminal study [90] which examined the motion of axisymmetric ellipsoidal particles immersed in a simple shear flow, there has been a significant amount of work devoted to experimental investigations of Jeffery's hypotheses [91, 92] and studies of effects of inertia [93, 94], particle-particles interactions [95], and Brownian motions [96, 97]. To take proper account of Brownian motion and particle-particle interactions in nanorod composites, the hydrodynamic model of Doi-Hess kinetic theory for sheared nematic polymers [75, 76] is adopted here. A brief recall of the formulation as in [73, 74] is presented in the following.

Denote the orientation of a rod by its axis of symmetry $\boldsymbol{m}$ and the probability distribution function (PDF) for its orientation by $f(\boldsymbol{m}, t)$. The dynamics of $f(\boldsymbol{m}, t)$ in a flow field $\boldsymbol{v}$ satisfy:

$$\begin{aligned} \frac{\partial f}{\partial t} + \boldsymbol{v} \cdot \nabla f &= \mathcal{R} \cdot [D_r^0(\mathcal{R} f + \frac{1}{kT} f \mathcal{R} V)] - \mathcal{R} \cdot [\boldsymbol{m} \times \dot{\boldsymbol{m}} f], \quad (3.2) \\ \dot{\boldsymbol{m}} &= \boldsymbol{\Omega} \cdot \boldsymbol{m} + [\boldsymbol{D} \cdot \boldsymbol{m} - \boldsymbol{D} : \boldsymbol{mmm}], \quad (3.3) \end{aligned}$$

where D_r^0 is the rotary diffusivity; k is the Boltzmann constant; T is absolute temperature; $\mathcal{R}$ is the rotational gradient operator $\boldsymbol{m} \times \frac{\partial}{\partial m}$; V is the mean-field, Maier-Saupe excluded-volume potential

$$\begin{aligned} V &= -\frac{3}{2} NkT \boldsymbol{mm} : \boldsymbol{M}, \\ \boldsymbol{M} &= \langle \boldsymbol{mm} \rangle = \int_{\|\boldsymbol{m}\|=1} \boldsymbol{mm} f(\boldsymbol{m}, t) d\boldsymbol{m}. \end{aligned}$$

The imposed flow $\boldsymbol{v}$ is a simple shear (Figure 3.1) with x being the flow direction, y being the flow-gradient direction, and z being the vorticity direction:

$$\boldsymbol{v}(x, y, z) = Pe(y, 0, 0);$$

$\boldsymbol{D}$ and $\boldsymbol{\Omega}$ are the corresponding rate-of-strain (symmetric) tensor and voticity (anti-symmetric) tensor of the flow $\boldsymbol{v}$.

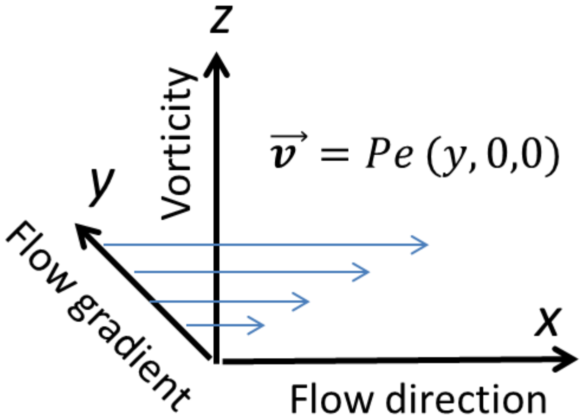

FIGURE 3.1. An illustration of the imposed shear flow with velocity field: $\vec{v} = Pe(y, 0, 0)$, i.e., the direction of flow is along the x axis, with y axis the flow gradient direction and z the vorticity direction.

Eq. (3.2) cannot be solved explicitly; however, its solution is well approximated by a spherical harmonic expansion,

$$f(\boldsymbol{m}, t) = \sum_{l=0}^{L} \sum_{n=-l}^{l} a_{l,n}(t) Y_l^n(\theta, \phi),$$

where Y_l^n are complex spherical harmonic functions and (θ, ϕ) are the spherical coordinates of the axis $\boldsymbol{m}$:

$$\boldsymbol{m} = (\sin\theta\cos\phi, \sin\theta\sin\phi, \cos\theta).$$

The spherical harmonic expansion renders Eq. (3.2) into a set of ordinary differential equations (ODE) for the coefficients a_l^n which can be easily solved numerically. Forest *et al.* [73, 74] showed that results are robust for a finite series expansion for $L \geq 10$. Similarly, in this work Eq. (3.2) is solved by numeric solution of the 65-dimensional ODE system resulting from truncating the spherical harmonic expansion at $L = 10$.

To gain insight into the distribution function $f(\boldsymbol{m}, t)$, 3000 sample points are draw from $f(\boldsymbol{m}, t)$ at different shear rate Pe. The sample points lie on the unit sphere S^2 indicating the direction of $\boldsymbol{m}$. Figure 3.2 plots the sample points in space viewed from top (left column) and viewed from side (right column) at 4 shear rates, from no shear (Pe=0) to strong shear (Pe=10). As shear increases, nanorods will be more likely to align with the flow direction (x axis), while slightly biased towards the shear direction (y axis) and more orthogonal to the vorticity direction (z axis). This anisotropy in orientation will be reflected in network properties such as anisotropic percolating paths and conductivities.

The distribution of $\boldsymbol{m}$ can be quantitatively characterized by its second moment tensor $\boldsymbol{M} = \int_{\|\boldsymbol{m}\|=1} \boldsymbol{m}\boldsymbol{m}f(\boldsymbol{m}, t)d\boldsymbol{m}$. The eigenvector associated with the largest eigenvalue of $\boldsymbol{M}$ corresponds to the principal direction of alignment (i.e., the most likely direction). When $Pe = 0$ (no shear) the three eigenvalues of $\boldsymbol{M}$ are $\{1/3, 1/3, 1/3\}$ and hence the orientation is isotropic. When $Pe > 0$ both asymptotic analysis [78] and numerical calculation [74] show that the largest eigenvector (i.e., the one corresponding to the largest eigenvalue) lies in the x-y plane, pointing approximately 45° from the x axis as $Pe \to 0^+$, and moves closer to the x axis as shear increases; the second eigenvector also lies in the x-y plane, and the smallest eigenvector aligns with z axis or the vorticity direction. These results agree with the observations in Figure 3.2.

3.2.3. Network Model. Every MC realization of a 3D nanorod dispersion is mapped to an undirected weighted network to study its linear DC electrical response. Recall that each MC realization distributes rods uniformly in space with orientations drawn from the specified single-particle orientation distribution. Electrically conducting contact between rods is assumed wherever rods overlap, that is, whenever their axes are within one rod diameter. To study percolation and conductance along each of the three physical dimensions, (perfectly) conducting plates are assumed at the two opposite faces of the box orthogonal to the specified dimension, corresponding to imposing a voltage drop across that dimension, with all intersections between rods and the selected boundary taken to be conducting. Working non-dimensionally, we treat each rod to be a conductor with unit conductivity. Then the conductance of a full rod is equal to its cross-sectional area divided by its length. For the purposes of the present model, we treat the matrix/solvent as a perfect insulator, noting that the typical ratio of conductivities is many orders of magnitude [48, 83, 84]. Every node in the corresponding electrical network represents

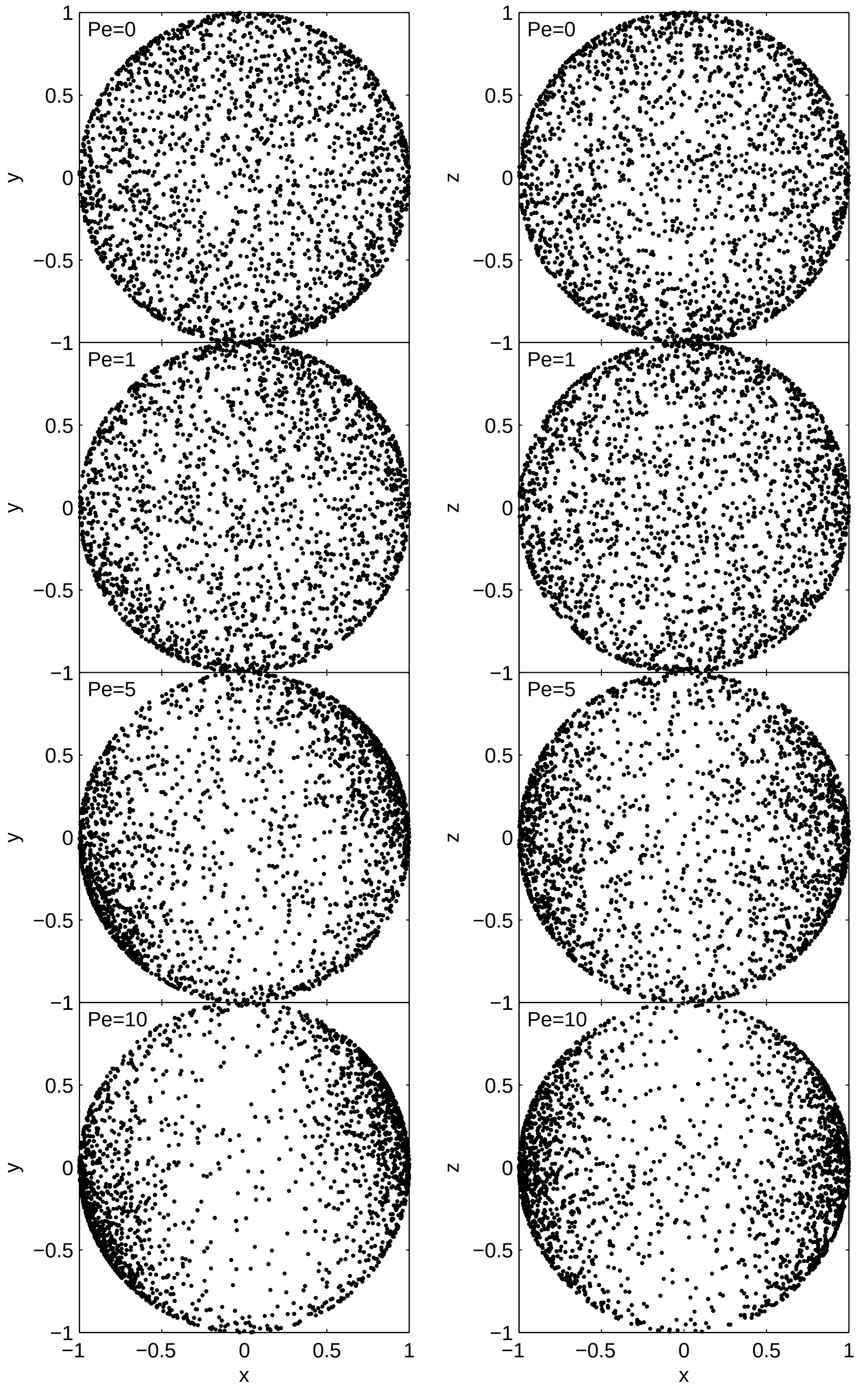

FIGURE 3.2. Plots of sample points $\boldsymbol{m}$ draw from $f(\boldsymbol{m}, t)$ viewed from top (left column) and viewed from side (right column) at 4 shear rates, from no shear (Pe=0) to strong shear (Pe=10). Each subplot contains 3000 points.

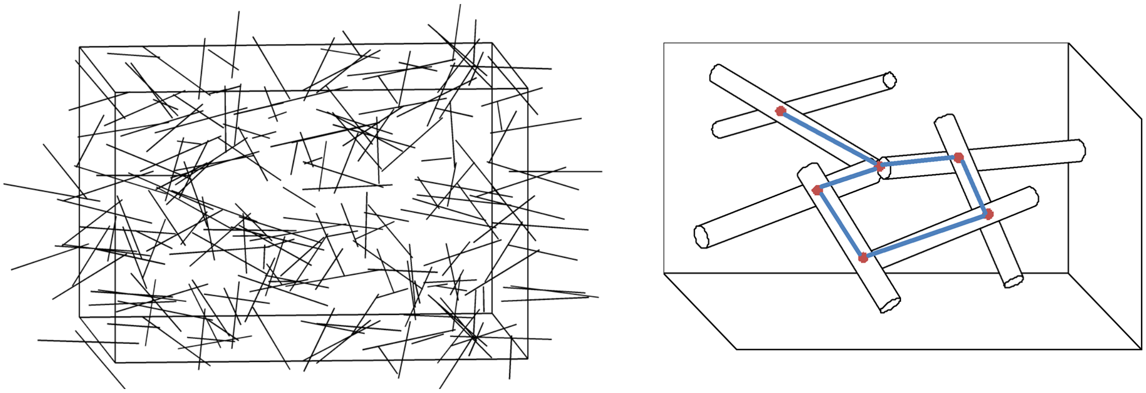

FIGURE 3.3. Left: A randomly oriented ($Pe = 0$) dispersion of aspect ratio 50 rods at volume fraction .0008. The box is four times the rod length. Right: An illustration of the network representation of a few rods. Nodes are contact points of rods (the red dots), and edges are the effective conductances between contact points (the blue lines).

one of the points of electrical contact between two rods or with a conducting plate, with weighted edges specified by the effective conductance between two contacts, inversely proportional to the corresponding distance along the rod connecting the two contact points (Figure 3.3 (Right)), as represented by the (symmetric) adjacency matrix $\boldsymbol{A}$:

$$A_{ij} = \begin{cases} w_{ij} & \text{if node i and node j are connected} \\ 0 & \text{otherwise} \end{cases}$$

with conductances $w_{ij} = s/d_{ij}$ given by the rod cross-sectional area, s, and the distance between node i and node j, d_{ij}. To investigate electrical conductivity in a specified direction, the conducting end plates placed on the corresponding opposite faces are each represented by a node, connected to one another through an external source.

Assuming the applied voltage is less than the dielectric breakdown strength and ignoring all inductance and electron tunneling effects, those clusters isolated from the external source will not be charged and hence only clusters containing the two plate nodes (i.e., a connected component containing all percolating paths) need to be considered. For each realized network obtained above, we use a Dulmage-Mendelsohn decomposition of the adjacency matrix to efficiently identify the connected components that contain the two plates. The next key ingredient in our calculation procedure is *the plate-constrained*

2-core — defined here as the connected subgraph containing both boundary plates with degree at least two in the subgraph. This plate-constrained 2-core captures all edges that potentially carry non-zero current in the posed problem. This pre-processing step provides two significant advantages. 1. Restriction to the plate-constrained 2-core filters approximately 90% of the edges near percolation threshold, therefore reducing the linear system to 10% of its original size (e.g., see the reduction at volume fraction 1.3% in the left panel of Figure 3.5). 2. By *a priori* elimination of all edges not in the plate-constrained 2-core, we remove a vast fraction of exactly zero-current edges from the numerical simulation of the linear system, thereby improving numerical precision overall, and in particular improved resolution of the small current tail. Therefore, we pass from the whole network to this plate-constrained 2-core and by slight abuse of terminology, we continue to represent its adjacency matrix by $\boldsymbol{A}$. More stringent reduction within single percolating paths could be achieved by application of further graph theoretic calculations, but such further reductions are deferred for the present results. We note that this result already informs that while a given volume fraction is necessary to statistically guarantee percolation, in fact on the order of 10% of the nanorods participate in the property gains.

The linear electrical response of this reduced network is given by Kirchoff's law (see, e.g., Strang [59]) $\boldsymbol{L}\boldsymbol{v} = \boldsymbol{f}$, where $\boldsymbol{v}$ is a vector indicating the voltage at each node, $\boldsymbol{f}$ is a vector consisting of the net current going out of each node, and $\boldsymbol{L}$ is the graph Laplacian matrix of the network. $\boldsymbol{L}$ is related to the adjacency matrix $\boldsymbol{A}$ by $\boldsymbol{L} = \boldsymbol{D} - \boldsymbol{A}$, with $\boldsymbol{D}$ a diagonal matrix containing the strength of each node ($D_{ii} = \sum_j A_{ij}$). For all internal nodes i, $f_i = 0$, while $f_{sink} = -f_{source} = I$ at the two nodes representing the source and sink at oppositely facing end plates.

The bulk conductance is the ratio of the external current to the obtained voltage drop across the two plate nodes, with bulk conductivity σ following by multiplying by the box's length L and dividing by its cross-sectional area L^2, that is, the bulk conductivity characterizes the macroscopic relationship between the total current passing between the two plates and the associated voltage drop. Naturally, if the two virtual nodes are not connected by a percolating path, the bulk conductivity in this model is zero. The current distribution inside the network also follows as part of this calculation. By Ohm's law, the current on an edge is equal to the voltage drop between its two endpoints multiplied by its effective conductance.

3.3. Results and Discussions

3.3.1. Monte Carlo Generation of Physical 3D Sheared Nanorod Dispersions.

For each fixed (Pe, θ) we create a physical 3D realization of the nanorod dispersion by drawing from the kinetic orientational distribution. Next we assess the corresponding electrical transport in each of the three spatial dimensions for each realization, obtaining the bulk conductivity for each realization and the underlying distribution of edge (rod) currents per realization. At the same (Pe, θ), we generate 1000 Monte Carlo realizations, and then average over all these 1000 realizations to obtain a statistical description of the electrical properties of a material volume of linear dimension 0.5 microns at each point (Pe, θ) of the phase diagram of Figure 3.5 (Right). Below we will make contact with the literature on bulk or mean properties first, then exploit our methods to drill into the multiscale properties in the rod phase, and finally show that the key bulk properties that are experimentally observed are consequences of our more detailed multiscale metrics.

The imposed flow is pure shear along the x axis, with y axis the flow gradient direction and z the vorticity direction (Figure 3.1). For the present results, we consider a model system of typical nanorods which are 1 nm × 50 nm, dispersed in an $L \times L \times L$ cubic domain. For consistently comparing results at different parameter values below, we choose the box length L to be 10 times the rod length (containing approximately $40,000$-$70,000$ rods for the range of the volume fractions studied in this paper), except for the finite size scaling analysis where we consider the effect of different box lengths (section 4.3.2).

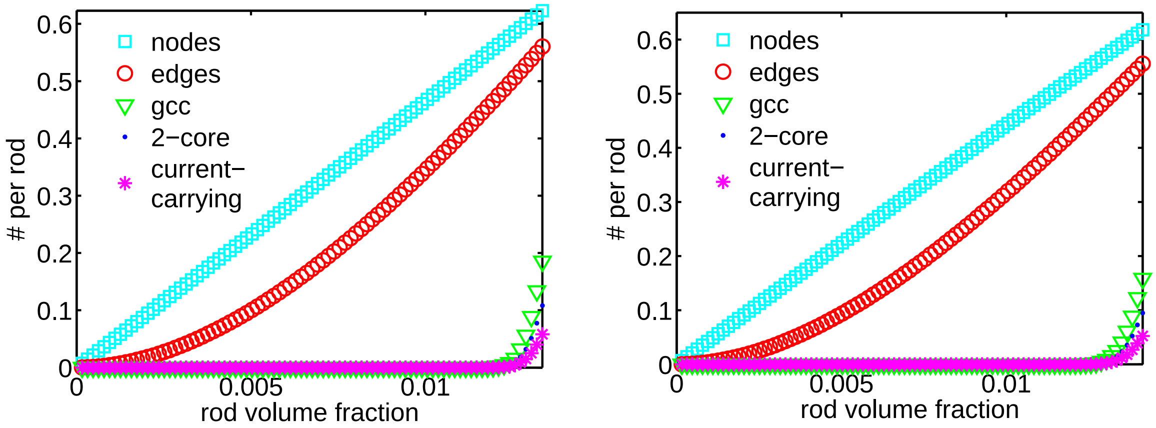

FIGURE 3.4. Average number of nodes in the network (square), number of edges in the network (circle), number of edges in the percolating component (triangle), number of edges in the plate-constrained 2-core (dot), number of current-carrying edges (star) as rod volume fraction varies. All the quantities are normailized by the average number of rods. The left panel corresponds to $Pe = 0$ and the right panel corresponds to $Pe = 5$.

Figure 3.4 (left) shows the size of the network normalized by the number of rods as rod volume fraction increases. The shear rate $Pe = 0$. When there are N rods, the number of contacts between rods will be proportional to N^2 since the rods are randomly placed and oriented. Therefore the number of nodes normalized by N is proportional to the rod volume fraction. However, the number of edges will be less in this model, because at least two contacts must be present on a rod in order to have an edge. If the two rods that intersect do not have contact with any other rod, then there will be one node but no edge. Around percolation threshold (which will be defined in the next section) the average degree of the network is larger than 1 (≈ 1.8). This is quite different from an Erdős-Réyni random graph because in our network the maximum degree of a node is only 4. The statistics for the network extracted from sheared ($Pe = 5$) dispersions are presented in the right panel of Figure 3.4. Shear decreases the probability of contact and consequently deceases the numbers. However, the scalings are qualitatively similar.

3.3.2. Dimensional Percolation. At each shear rate Pe, we calculate the critical rod volume fraction for percolation $\theta_c(L) = \int \theta \, dR_L$ (i.e., the effective percolation threshold as defined in [1] for a finite system with linear size L) for each of the three physical directions, where the percolating probability, $R_L(\theta)$, is approximated by the fraction of percolated samples out of 1000 realizations. We then plot the percolation thresholds for each of the three physical dimensions against shear rate Pe in the right panel of Figure 3.5 and reproduce the percolation phase diagram in Zheng *et al.*, Figure 4 [2] over a smaller domain but with higher resolution. As previously described, alignment of nanorods decreases the probability of contact, thus increasing the percolation thresholds, and the influence of shear on percolation threshold depends on the direction being considered, resulting in the observed dimensional percolation contrasts. In the right panel Figure 3.5 there is no percolation (statistically) in the region below the solid curve; percolation appears in the flow (x) direction in the region between the solid curve and the dashed curve; in the region between the dashed curve and the dotted curve, percolation emerges in the flow gradient (y) direction in addition to the flow (x) direction; above the dotted curve, percolation spans all three dimensions. We note that the percolation thresholds appear to be linearly dependent on the normalized shear rate Pe over most of the range of Figure 3.5 (Right).

3.3.3. Anisotropic Bulk Conductivity. To elucidate the effect of shear on the scaling of conductivities, we first take 2 slices in the right panel of Figure 3.5 at $Pe = 0$ and $Pe = 5$. Figure 3.6 plots the mean conductivity σ in each of the three directions against rod volume fraction $\theta - \theta_c$ for isotropic ($Pe = 0$) dispersions (left) and sheared ($Pe = 5$) dispersions (right). Figure 3.6 demonstrates that *the power-law scaling of conductivity σ persists under shear with scaling exponents along each physical axis tuned by the shear rate Pe*. Therefore we propose a general scaling form with shear:

$$\sigma \sim (\theta - \theta_c(Pe))^{t(Pe)}, \tag{3.4}$$

where the scaling exponent $t(Pe)$ varies with the direction in physical space, i.e., $t_x(Pe)$, $t_y(Pe)$, $t_z(Pe)$ are distinct. Here we focus on the three physical directions: flow direction (x), flow gradient direction (y), and vorticity direction (z). At each normalized shear rate Pe, we fit Equation 3.4 to the mean conductivity in each direction as in Figure 3.6,

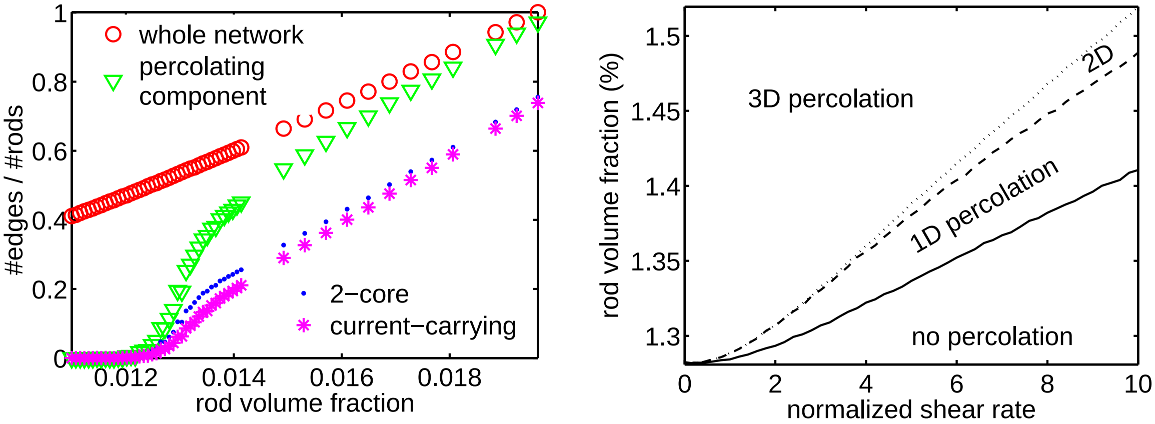

FIGURE 3.5. Left: The average number of edges in the rod contact network (circle), in the percolating components (triangle), in the plate-constrained 2-core (dot), and in the current-carrying paths (star), normalized by the total number of rods at each rod volume fraction. Rods are isotropically oriented ($Pe = 0$). Thus restriction to the plate-constrained 2-core filters approximately 90% of the rods near percolation threshold $\theta_c \doteq 1.3\%$, therefore reducing the problem to 10% of its original size. Right: Percolation phase diagram with anisotropic percolation thresholds in the 2-parameter space of (Pe, θ) (cf. Figure 4 in [2]). The solid, dashed and dotted curves correspond to the percolation thresholds in the x, y and z directions, respectively.

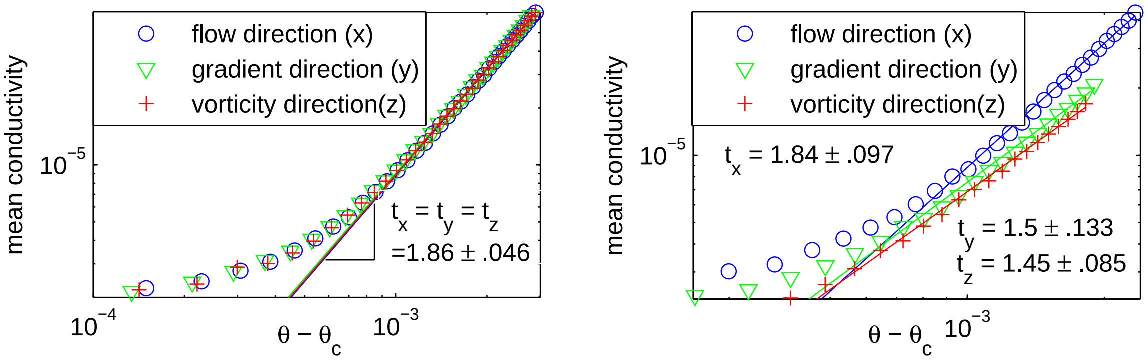

FIGURE 3.6. Scaling of the mean conductivity σ in each of the three directions against rod volume fraction $\theta - \theta_c$ for isotropic ($Pe = 0$) dispersions (left) and sheared ($Pe = 5$) dispersions (right). The power-law scaling of conductivity persists under shear, while the scaling exponent is anisotropic for $Pe > 0$. Each data point is the average of 1000 realizations in a cubic box of linear dimension 0.5 microns (10 times the nanorod length).

and plot the scaling exponents in Figure 3.7 against Pe. While shear diminishes the conductivity exponents (and hence diminishes the property gains) in general, it has the

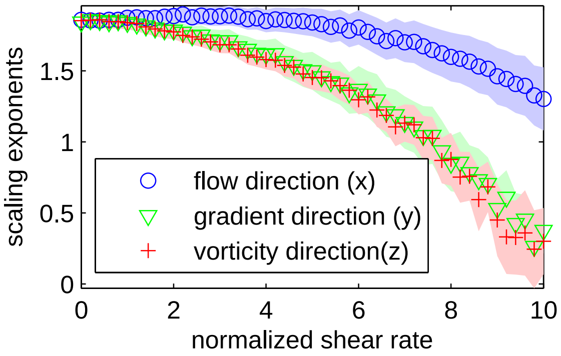

FIGURE 3.7. Anisotropic conductivity exponents against normalized shear rate Pe. The scaling exponents are estimated from fitting Equation 3.4 to the mean conductivity in each direction. A 95% confident interval is shown as a shaded region around each exponent.

least impact in the flow direction. The conductivity exponents $t(Pe)$ are approximately quadratic functions of Pe, as can be calculated from the data in Figure 3.7:

$$\begin{aligned} t_x &\approx 1.83 + 0.053Pe - 0.01Pe^2, \\ t_y &\approx 1.83 + 0.018Pe - 0.017Pe^2, \\ t_z &\approx 1.83 + 0.02Pe - 0.018Pe^2. \end{aligned} \tag{3.5}$$

3.3.4. Scaling of Current Distributions. In a previous study [30], we analyzed global features of the current distribution on a cubic lattice (i.e., bond percolation) and identified a robust, exponential large current tail that persists above threshold and is locally independent of the bond fraction. Here we perform similar analysis on the current distribution in physical 3D nanorod dispersions, and show that similar scaling behavior arises in these more complex systems even though the centers of mass of the nanorods are random, the distances between nodes in the percolating clusters are highly non-uniformly distributed, and the percolating network is spatially anisotropic.

3.3.4.1. *Robust Exponential Tail of Current Distributions.* Figure 3.8 plots current distributions (left) and logarithmic current distributions (right) for isotropic ($Pe = 0$) dispersions at various rod volume fractions θ above threshold $\theta_c \doteq 1.3\%$, given a unit voltage

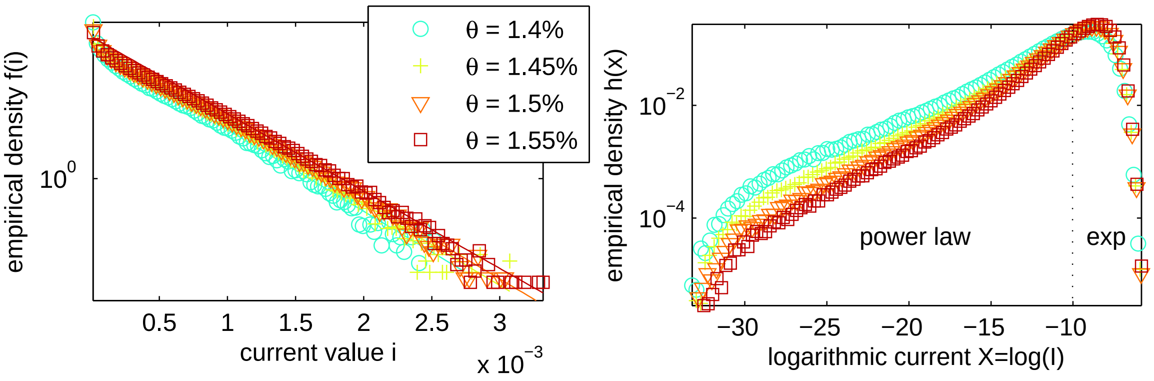

FIGURE 3.8. Current distributions $f(i)$ (left) and logarithmic current distributions $h(x)$ (right) for isotropic ($Pe = 0$) dispersions at various rod volume fractions θ given a unit voltage source. The logarithmic transformation of currents exposes small currents which have a power law distribution (right panel) while the overall current distribution is exponential (left panel). The empirical densities are derived from the histograms of all the currents over 1000 realizations.

source. Since the current distributions in all three directions are statistically similar as the rods are isotropically oriented, only the current distribution in the flow direction (x) is shown. Let $f(i)$ be the probability density function (PDF) of the currents across the population of current-carrying edges (i.e., ignoring zero-current edges where present) and $h(x)$ be the corresponding PDF of the logarithmic current $X = \ln(I)$. The two distributions are related by $h(x) = f(e^x)e^x$.

First, the logarithmic transformation of current (Figure 3.8 (Right)) exposes the small current region and reveals the power-law distribution of small currents, agreeing with what has been reported for bond percolation on a cubic lattice [30, 44–46]. For relatively large currents (i.e., to the right of the peak of the $h(x)$ distribution), Figure 3.8 (left) is clearly suggestive of an exponential tail of the current distributions which expands broadly over large to moderate currents and dominates the current distribution at the expense of the vanishing power law scaling in the small current tail.

The second conclusion drawn from Figure 3.8 is that the rate of the exponential tail above threshold is weakly dependent on the rod volume fraction θ near threshold given a unit voltage source, despite the fact that the current distribution close to the percolation threshold $\theta_c \doteq 1.3\%$ shows some scattering because of the finite size effect. In [30] we

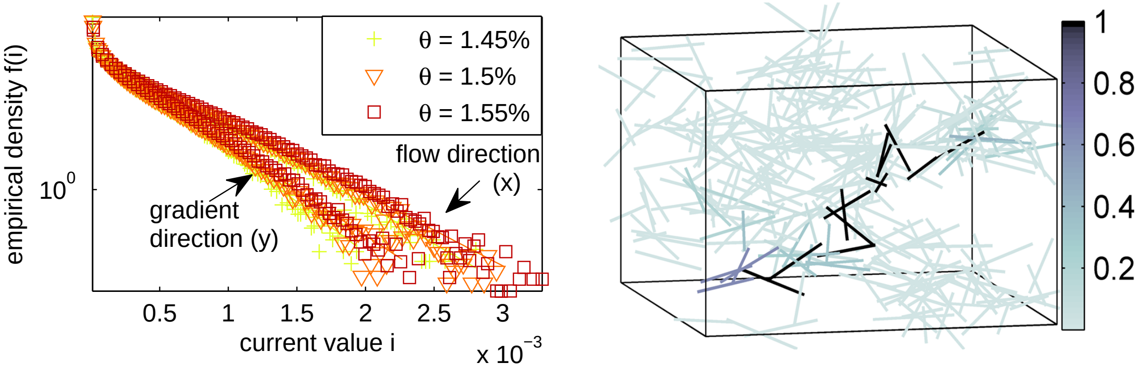

FIGURE 3.9. Left: Current distributions in both the flow direction (x) and the flow gradient direction (y) for sheared dispersions ($Pe = 5$). The percolation threshold is $\theta_c(x) \doteq 1.35\%$ in the flow direction (x) and $\theta_c(y) \doteq 1.4\%$ in the flow gradient direciton (y). Right: Visualization of the current-carrying rods and color-coded current values in a percolating cluster in the x direction from one realization at (Pe, θ)=(10, .015).

quantitatively confirmed the independence of the exponential tail on bond density on cubic lattices, and showed the convergence to a robust class of exponential distributions for the large current tail both near and above threshold.

In order to study the effect of shear, we plot the current distributions in both the flow direction (x) and the flow gradient direction (y) for sheared dispersions ($Pe = 5$) in the left panel of Figure 3.9. We omit the current distributions in the vorticity direction (z) for clarity because they almost overlap with the distributions in the y direction. (In weak shear it is known that the principal axis of the rod orientational distribution is approximately along the 45 degree line in the shear plane [74].) Because of the shear-induced anisotropic rod orientation, the current distributions are likewise anisotropic and the shear rate selects the exponential rates of the distributions. However, the robust exponential tail, which dominates the current distribution above threshold, persists in each spatial direction and is weakly dependent on the rod volume fraction θ as in the isotropic ($Pe = 0$) case.

Mathematical reasoning for the existence of the exponential tail remains unknown. The intuition behind the exponential tail is that large currents are very rare while small currents are more abundant. We also note that the exponential cut-off in the cluster size distribution [39] may very well be related, as suggested by our colleague Michael Rubinstein, yet this remains an open problem. Importantly, the small numbers of large currents in the tail of the distribution of current-carrying rods exacerbates the separate phenomena of there being relatively few current-carrying rods among the total dispersion, as remarked on above (see the left panel of Figure 3.5). To illustrate the combined effect of small numbers of current-carrying rods and even smaller numbers of large currents, Figure 3.9 (Right) visualizes the currents flowing in the x direction in a single Monte Carlo realization of a 3D sheared dispersion, at $(Pe,\theta)=(10, .015)$ and box length $L = 250\ nm$, demonstrating how very few of the approximately 10^5 rods in this volume carry the largest currents. This result compels a further study of the stability of percolating components under small strain deformations, since such conditions arise in many thin film applications.

3.3.4.2. *Finite Size Scaling Analysis.* Thus far we have considered the electrical response to a unit voltage source in a finite system of length L. To meaningfully describe the current distribution in an infinite system ($L \to \infty$) and to better understand the effect of system size on the distribution, we perform a finite size scaling analysis as in [30]. Let $f_L(i)$ be the PDF of the current at system size L for a unit voltage source. We propose a finite-size scaling form:

$$L^{-u} f_L(L^{-v} i) = f^{\infty}(i), \tag{3.6}$$

where f^{∞} is a function independent of L. By tuning u and v we aim to eliminate the effect of system size. Figure 3.10 (left) plots the current distributions in isotropic dispersions (Pe=0) at rod volume fraction $\theta = 1.33\%$ for different system sizes. The inset confirms that the PDF's for different system sizes collapse onto a single curve when $u = 1$ and $v = 1$. One can carry out the same argument at other rod volume fractions above threshold $\theta_c \doteq 1.3\%$ and find the same scaling exponents. In other words, f^{∞} can be viewed as the limiting current distribution for system size L and external voltage source $V^* = L$ (i.e., a unit electric field). This simple scaling form indicates that M_k, the k-th

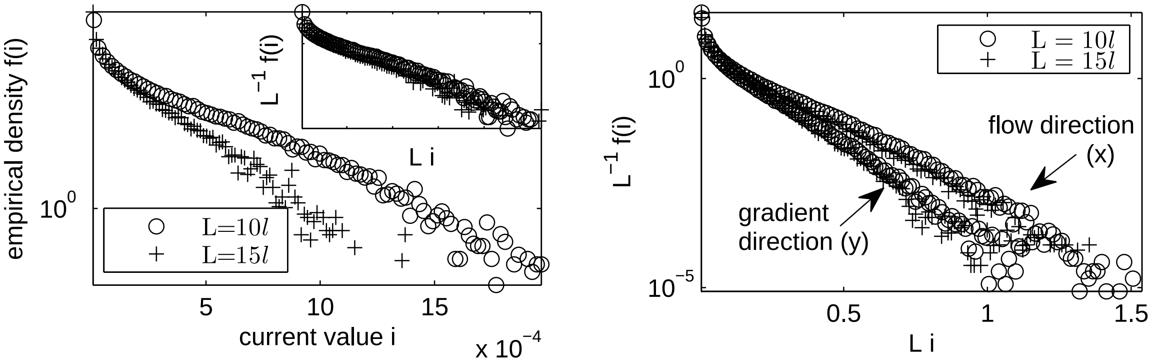

FIGURE 3.10. Left: current distributions in isotropic dispersions ($Pe = 0$) at rod volume fraction $\theta = 1.33\%$. Two system sizes are considered: 10 times as long as a rod ($L = 10l$) and 15 times as long as a rod ($L = 15l$). The inset shows the same distributions rescaled by the system size L with $u = 1$ and $v = 1$. Right: rescaled current distributions in the flow direction (x) and in the flow gradient direction (y) in sheared ($Pe = 5$) dispersions at rod volume fraction $\theta = 1.5\%$. It demonstrates that the finite size scaling form Equation 3.6 holds in each direction under shear.

moment of the current distribution, is a simple scaling function of L:

$$M_k = \int_0^\infty i^k f_L(i)\, di = \int_0^\infty i^k L\, f^\infty(Li)\, di \propto L^{-k}. \tag{3.7}$$

In [30] we showed that while this scaling of moments is not exact because of small currents which are multifractal, for large moments the exponential tail becomes dominant and Equation 3.7 is a good approximation.

Again this simple finite size scaling form Equation 3.6 remains the same in each direction under shear regardless of the current distribution being anisotropic, as shown in Figure 3.10 (Right) which plots the rescaled current distributions $f^\infty = L^{-1} f_L(L^{-1} i)$ in both the flow direction (x) and the flow gradient direction (y) for a sheared ($Pe = 5$) dispersion.

3.3.5. Electrical Property Phase Diagrams. The above arguments show that the power-law scaling of bulk conductivities near threshold persists under shear, and demonstrate a robust exponential tail of current distributions above threshold in response to a unit voltage source, even under shear. To conclude, *we paint the average bulk conductivities and the rates of the exponential current tails onto the percolation phase diagram*

(Figure 3.5 (Right)) in Figure 3.11. From left to right, the top three panels in the figure show the color-coded average bulk conductivities in the flow (x) direction, flow-gradient (y) direction, and vorticity (z) direction respectively; and the bottom three panels show the rates of the exponential current tails in the three physical directions respectively. The effect of shear on the conductivities are similar while shear has relatively smaller impact in the flow (x) direction. However, the exponential current tails present qualitatively different behaviors. In the flow (x) direction, the exponential rate drops as shear increases, i.e., the tail becomes fatter, indicating that large currents are more frequent in the flow direction as shear increases. By contrast, in both the flow gradient (y) and the vorticity (z) directions the exponential rates increase with shear rate, meaning thinner tails, indicating that large currents are more rare in the plane normal to the flow direction as shear increases. This result is supported by asymptotic results [74] on the weak shear limit that show for small Pe, the peak of the orientational PDF aligns with the 45° axis in the shear plane (x,y), and then progressively tilts toward the flow (x) axis as Pe increases, always remaining in the shear plane for the low volume fractions relevant to percolation threshold. Thus the anisotropy in the large tail currents are strongly correlated with the orientational PDF of the rod phase.

Finally, we recall scaling analysis from our recent paper [30] on random resistor networks in cubic bond percolation. From the established exponential large current tail across the percolation phase diagram (Figure 3.11, bottom row), two results immediately follow. First, the largest current in the network scales as $\ln(L)$. Note that previous studies on the largest current in lattice bond percolation [53–56] do not analyze the tail of the current distribution, and there are infinitely many tails consistent with the logarithmic scaling of the maximum current. Knowing the tail is exponential, however, immediately implies the scaling of the maximum current. Second, since the second moment of the current distribution relates to the bulk conductivity, the celebrated power law scaling of measured bulk conductivity is a consequence of the large current exponential tail. Specifically, given a unit external voltage source, the bulk conductance C is related to the current distribution by [30]

$$C/N = \sum_b i_b^2 r_b / N = \int_0^\infty i^2 r f(i,r)\, di dr, \tag{3.8}$$

where the sum is taken over all edges with nonzero current, i_b and r_b are the current value and the resistance of edge b, respectively, and N is the number of edges with nonzero current. Assuming that the current distribution and the edge resistance distribution are weakly dependent, the joint distribution $f(i,r)$ can be approximated by the product of individual distributions $f_I(i)$ and $f_R(r)$, and Equation (3.8) yields $C/N \approx \langle r \rangle \int_0^\infty i^2 f_I(i)\, di$. Since the second moment of the current distribution is dominated by the exponential large current tail, the power law scaling of the bulk conductance with respect to rod volume fraction θ is revealed by the scaling behaviors of the exponential current tail, the mean edge resistance and the number of edges with large current. In other words, the observable bulk properties (e.g., Equation (3.4) and (3.5)) can be reconstructed from particle-scale property distributions (e.g., the exponential large-current tail of the current distribution and mean edge resistance). These observations are relevant especially to “active” composite materials where materials are exposed to mechanical loading and strain deformations.

3.3.6. Properties along Eigenvector Directions. The results and analyses above are for the three physical directions (i.e., x-flow direction, y-flow gradient direction, and z-vorticity direction), which are natural choices since properties in these directions are easy to measure in the lab frame. However, the eigenvectors of the second moment tensor $\boldsymbol{M}$ of the orientational distribution function $f(\boldsymbol{m}, t)$ (see section 3.2.2) suggest a different reference frame, which might be less intuitive but is intrinsic to the orientational distribution function. Denote the three eigenvalues of $\boldsymbol{M}$ by $\lambda_1 \geq \lambda_2 \geq \lambda_3$ and the corresponding eigenvectors by v_1, v_2, and v_3, respectively. Figure 3.12 superimposes the percolation thresholds in the eigenvector directions v_1, v_2, and v_3 onto the percolation phase diagram in lab frame (Figure 3.5). v_1 is the most likely orientation of rods and hence the percolation threshold in this direction is always the lowest. Note that the percolation

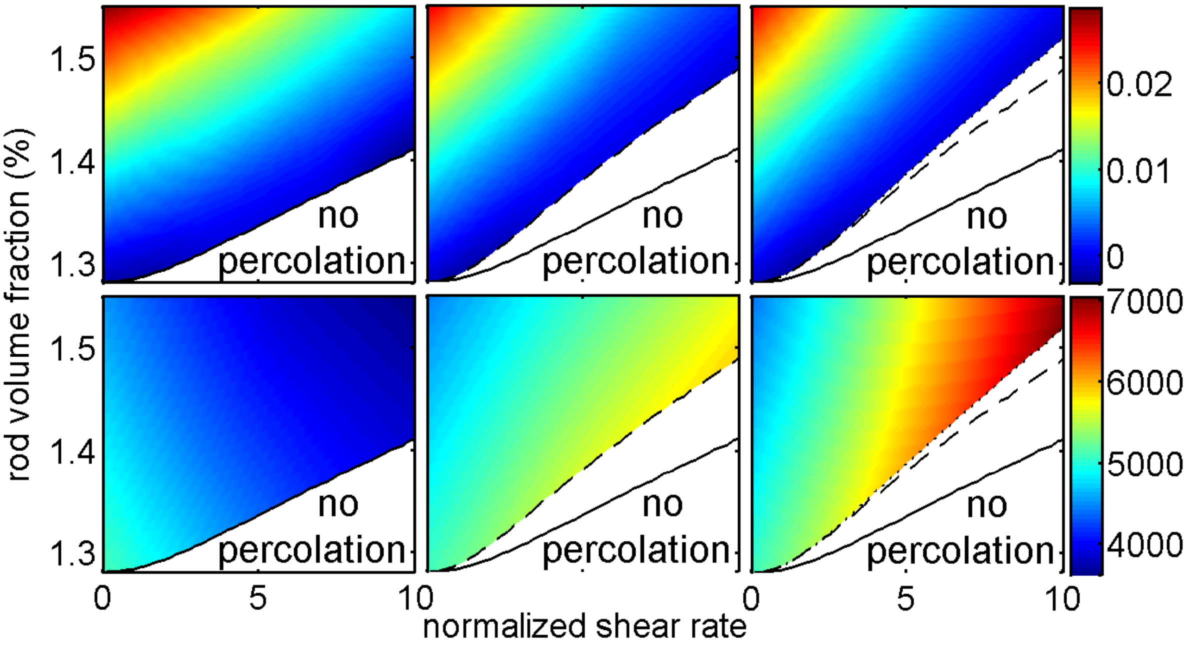

Figure 3.11. Multi-scale electrical properties across the percolation phase diagram (Figure 3.5 (Right)). The top row shows the **color-coded average bulk conductivities** in the flow (x) direction (left panel), flow-gradient (y) direction (center panel), and vorticity (z) direction (right panel). The bottom row shows the **rates of the exponential current tails** in the three physical directions respectively.

threshold in direction v_1 decrease in $0 < Pe < 1$, implying that very weak alignment actually increases the chance of contact of rods and therefore lowers the percolation threshold, which is a feature not seen in the lab frame. The second key observation is that the order of percolation switches as shear increases. When $Pe < 5$, the rod phase percolates in the v_3 direction before v_2 direction, while the order is reversed when $Pe > 5$. This apparent contradiction with the percolation order in the lab frame deserves further study.

The scaling behavior of bulk conductance and the exponential tail of the current distribution in the eigenvector directions are similar to their counterparts in the lab frame; therefore they are not included here.

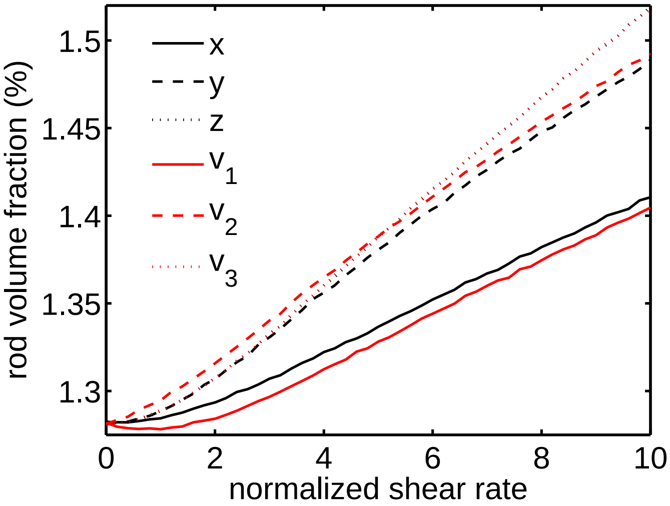

FIGURE 3.12. Percolation phase diagram with anisotropic percolation thresholds in the 2-parameter space of (Pe, θ) (cf. Figure 3.5). The black solid (x), dashed (y) and dotted (z) curves correspond to the percolation thresholds in the x, y and z directions, respectively; and the red solid (v_1), dashed (v_2) and dotted (v_3) curves correspond to the percolation thresholds in the eigenvector directions v_1, v_2, and v_3, respectively.

3.4. Conclusion

In summary, we construct a network representation to efficiently and accurately calculate the linear electrical response on percolating anisotropic nanorod dispersions in 3D across the phase diagram of rod volume fraction and imposed normalized shear rate associated with a thin film flow. The dispersions are generated from pre-computed orientational probability distributions across the phase diagram [73, 74]. Network methods provide an efficient algorithm to identify the current-carrying rods in percolating nanorod components, combining with Monte Carlo calls to the orientational distributions to deliver robust, multi-resolution distributions of conductivity consistent with the statistical properties of the underlying nanorod ensembles. Putting these tools together, we statistically investigate electrical properties on the sheared nanorod percolation phase diagram of [2]. For each data point in the phase diagram, we determine the mean and variance of the bulk conductivity as well as current distributions within percolating rod clusters, with the ability to identify current values at the rod scale in each 3D physical realization. The numerical results show that the celebrated power-law scaling of conductivity above percolation threshold persists under shear, even while the conductivity becomes anisotropic due to the sheared nanorod orientational distribution. Furthermore, we show that the anisotropic power-law scaling in the observable bulk conductivity tensor is a consequence of a deeper transport property within the network. Namely, there is a robust exponential, large current tail in the current distribution throughout the nanorod phase; the exponential tails imply the conductivity scaling by taking second moments of the current distribution. We compute the large current tails, and exponential rates, across the phase diagram of nanorod volume fraction and normalized shear rate. Remarkably, at approximately 1.3% rod volume fraction, the percolating dispersions typically yield mean conductivities that are only 4 orders of magnitude lower than the pure rod phase. The volume averaged boost in conductivity for the same parameters [2] is negligible compared to this percolation effect.

CHAPTER 4

Evolving Voter Model with Two Opinions

4.1. Introduction

In recent years, a variety of research efforts from different disciplines have combined with established studies in social network analysis and random graph models to fundamentally change the way we think about networks. Significant attention has focused on the implications of dynamics in establishing network structure, including preferential attachment, rewiring, and other mechanisms [8, 23–26]. At the same time, the impact of structural properties on dynamics on those networks has been studied [27], including the spread of epidemics [7, 98–100], opinions [101–103], information cascades [104–106], and evolutionary games [107, 108]. More recently there has been a number of studies of systems in which the states of individuals and the connections between them coevolve [29, 109]. The systems considered include evolutionary games [110–114] and epidemics [115–119], but the concentration here is on the spread of opinions [120–124]. Different from the models of cascades [19, 104, 125] which are also widely used in the study of opinion spread, the evolving voter model allows an agent to switch between different opinions and the network topology to change accordingly, yet it is assumed that agents impose equal influence over each other (cf. multi-state complex contagions [126–128]). This model provides building blocks to quantitatively study collective behaviors in various social systems, e.g., segregation of a population into two or more communities with different political opinions, religious beliefs, cultural traits, etc.

The starting point is the model proposed by Holme and Newman [34]. In their model there is a network of N vertices and M edges. The individual at vertex v has an opinion $\xi(v)$ from a set of G possible opinions and the number of people per opinion

$\gamma_N = N/G$ stays bounded as N gets large. On each step of the process, a vertex x is picked at random. If its degree $d(x)$ equals 0, nothing happens. If $d(x) > 0$, (i) then with probability $1 - \alpha$ a random neighbor y of x is selected and the opinion of vertex x is set to $\xi(x) = \xi(y)$; (ii) otherwise (i.e., with probability α) an edge attached to vertex x is selected and the other end of that edge is moved to a vertex chosen at random from those with opinion $\xi(x)$. This process continues until the 'consensus time' τ, at which there are no longer any discordant edges—that is, there are no edges connecting individuals with different opinions.

For $\alpha = 1$, only rewiring steps occur, so once all of the M edges have been touched, the graph has been disconnected into G components, each consisting of individuals who share the same opinion. Since none of the opinions have changed, the components of the final graph are all small (i.e., their sizes are Poisson with mean γ_N). By classical results for the coupon collector's problem, this requires $\sim M \log M$ updates, see e.g., page 57 in [129]. In the case of sparse graphs considered here $M \sim cN$ (i.e., $M/N \to c$) so the number of steps is $O(N \log N)$, i.e., when N is large it will be $\approx cN \log N$.

In contrast, for $\alpha = 0$ this system reduces to the voter model on a static graph. If the initial graph is an Erdős-Rényi random graph in which each vertex has average degree $\lambda > 1$, then (see e.g., Chapter 2 of [102]) there is a giant component that contains a positive fraction, μ, of the vertices and the second largest component is small having only $O(\log N)$ vertices. The voter model on the giant component will reach consensus in $O(N^2)$ steps (see, e.g., Section 6.9 of [102]), so the end result is that one opinion has μN followers while all of the other groups are small.

Using simulation and finite size scaling, Holme and Newman [34] showed that there is a critical value α_c so that for $\alpha > \alpha_c$ all of the opinions have a small number of followers at the end of the process, while for $\alpha < \alpha_c$ "a giant community of like-minded individuals forms." When the average degree $\lambda = 2M/N = 4$ and the number of individuals per opinion $\gamma_N \to 10$, this transition occurs at $\alpha_c \approx 0.46$. See [130–133] for recent work on this model.

4.2. Evolving Voter Model with Two Opinions

The model studied here differs from that of Holme and Newman in a number of ways. There are only two opinions (namely 0 and 1) instead of a number proportional to the size of the graph. On each step, a discordant edge connecting voters that disagree, rather than a vertex, is chosen at random and is given a random orientation, (x, y), avoiding the problem of picking vertices with degree zero or vertices that agree with all of their neighbors. Then with probability α vertex x breaks its edge to y and reconnects to (a) a vertex chosen at random from those with opinion $\xi(x)$ as in Holme and Newman, a process labeled as 'rewire-to-same', or (b) at random from the graph, a process labeled as 'rewire-to-random'; otherwise (i.e., with probability $1 - \alpha$), the voter at x adopts the opinion of the voter at y (i.e., set $\xi(x) = \xi(y)$). The process continues until there are no discordant edges.

4.2.1. Phase Transition. Suppose, for concreteness, that the initial social network is an Erdős-Rényi random graph in which each individual has average degree $\lambda > 1$, and that vertices are assigned opinions 1 and 0 independently with probabilities u_0 and $1-u_0$.

Despite the differences in implementation, the rewire-to-same model has a phase transition similar to that of Holme and Newman. In particular, the final fraction ρ of voters with the minority opinion undergoes a discontinuous transition at a value α_c that does not depend on the initial density as α varies. Figure 4.1 (left) shows results of simulations for the rewire-to-same model starting from Erdős-Rényi random graphs with $N = 100,000$ vertices and average degree $\lambda = 4$. Opinions are initially assigned randomly with the probability of opinion 1 given by $u_0 = 0.5$, 0.4, 0.3, 0.2 and 0.1. The figure shows the final fraction ρ of voters with the minority opinion for each u_0 and α. For $\alpha > \alpha_c \approx 0.44$, it suggests that $\rho \approx u_0$ and for $\alpha < \alpha_c$, $\rho \approx 0$.

The single difference in the rewiring step in the rewire-to-random model leads to fundamentally different model behaviors, as seen in Figure 4.1 (right), showing simulation results for the rewire-to-random model on initial Erdős-Rényi graphs with $N = 100,000$ nodes and average degree $\lambda = 4$ for $u_0 = 0.5$, 0.4, 0.3, 0.2, and 0.1. When $u_0 = 0.5$,

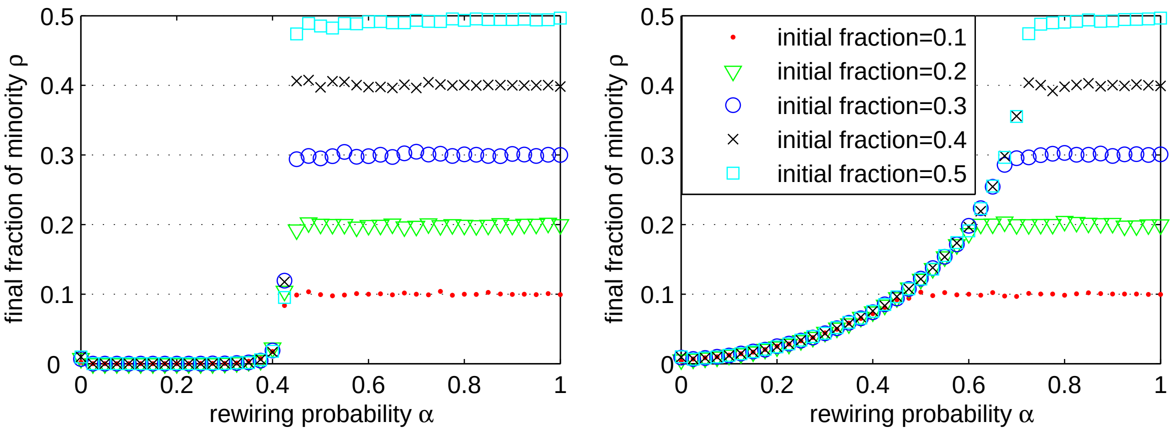

FIGURE 4.1. Fraction ρ of voters with the minority opinion in consensus state for the rewire-to-same model (left) and the rewire-to-random model (right). Phase transitions are observed in both models as the rewiring probability α varies. Simulations start from Erdős-Rényi random graphs with $N = 100,000$ vertices and average degree $\lambda = 4$. Opinions are initially assigned randomly with the probability of opinion 1 given by $u_0 = 0.5$, 0.4, 0.3, 0.2, and 0.1.

the final fraction ρ of voters with the minority opinion is constant at 0.5 over $[\alpha_c(0.5), 1]$ and then decreases continuously to a value near zero as α decreases to zero. For each initial density $u_0 < 0.5$ there exists a critical value $\alpha_c(u_0)$, so that the ending density $\rho(\alpha, u_0)$ stays constant at u_0 until the flat line (α, u_0) hits the curve $\rho(\alpha, 0.5)$ and then $\rho(\alpha, u_0) \approx \rho(\alpha, 0.5)$ for $\alpha < \alpha_c(u_0)$. Because all of the $\rho(\alpha, u_0)$ agree with $\rho(\alpha, 0.5)$ when they are less than u_0, the graph of $\rho(\alpha, 0.5)$ on $[0, \alpha_c(0.5)]$ is called *the universal curve.*

To further describe the phase transitions, Figure 4.2 plots the average time to consensus at each α for the rewire-to-same model (left) and the rewire-to-random model (right), showing the same behavior for the phase transitions as in Figure 4.1. In addition, Figure 4.2 distinguishes the time scales for the two different dynamics: voting is slow (requiring $O(N^2)$ steps to consensus) while rewiring is fast (requiring only $O(N \log N)$ steps to consensus). The voting dynamic dominates when $\alpha < \alpha_c(u_0)$ and the rewiring dynamic takes over when $\alpha > \alpha_c(u_0)$, yielding the phase transitions seen above.

To confirm that the phase transition at α_c for the rewire-to-same model is a discontinuity but not a sharp transition under-resolved by the simulation, Figure 4.3 (left) amplifies the region around the critical value $\alpha_c \approx 0.43$ and plots the results for three

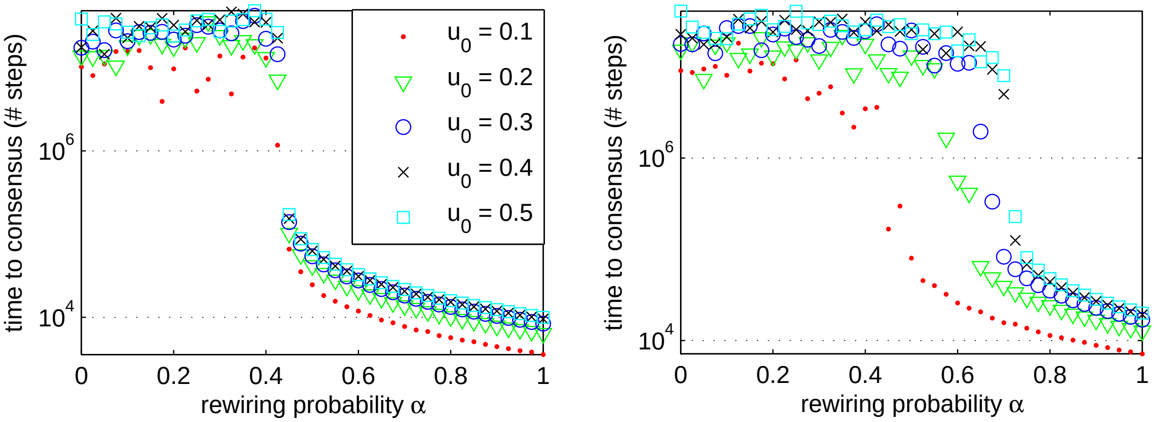

FIGURE 4.2. Average time to consensus as the rewiring probability α varies for the rewire-to-same model (left) and the rewire-to-random model (right), showing the same behaviors for the phase transitions as in Figure 4.1. Each data point in the figure is an average over 100 simulations starting from Erdős-Rényi random graphs with $N = 10,000$ vertices and average degree $\lambda = 4$. Opinions are initially assigned randomly with the probability of opinion 1 given by $u_0 = 0.5$, 0.4, 0.3, 0.2, and 0.1.

different graph sizes $N = 5,000$, $10,000$ and $20,000$. Figure 4.3 (right) shows the corresponding finite size scaling result. The three curves correspond to different system sizes cross at approximately $\alpha - 0.43 = 0$ (i.e., $\alpha_c = 0.43$), and they collapse for $\alpha < 0.43$. This indicates the following finite size scaling form:

$$\rho N = F(\alpha - 0.43), \tag{4.1}$$

where $F(\cdot)$ is a function independent of the system size. Therefore, $\rho \sim 1/N \to 0$ as $N \to \infty$ for $\alpha < \alpha_c$, and $\alpha_c \approx 0.43$. The seemingly continuous sharp transition is a finite size effect, and the transition approaches a discontinuity as $N \to \infty$. Further explanations for the nature of the transitions are presented in the following sections along with heuristic arguments for the universal curve $\rho(\alpha, 0.5)$ on $\alpha < \alpha_c(0.5)$ in the rewire-to-random model.

The conclusion drawn from this section is that the system has the following

Phase transition. *For each initial density $u_0 \le 1/2$ there is a critical value $\alpha_c(u_0)$ so that for $\alpha > \alpha_c(u_0)$, consensus occurs after $O(N \log N)$ updates and the fraction of voters*

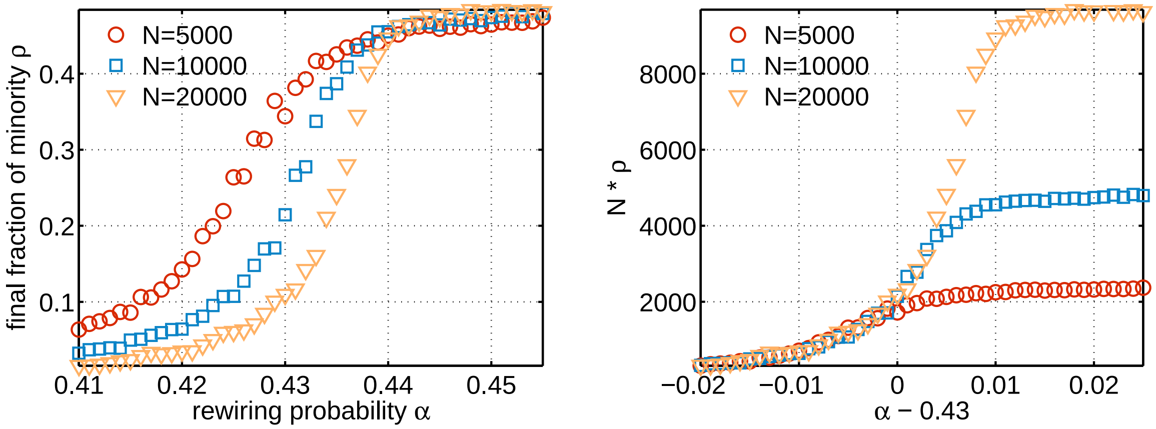

FIGURE 4.3. Left: Fraction ρ of voters with the minority opinion in consensus state as the rewiring probability α varies in the region near the phase transition point $\alpha_c \approx 0.43$ for the rewire-to-same model. Results for three different graph sizes $N = 5,000$, $10,000$ and $20,000$ are shown and initial fraction of the minority $u_0 = 0.5$. Right: The same plots as in the left panel rescaled by the system size. The three curves correspond to different system sizes cross at approximately $\alpha - 0.43 = 0$ (i.e., $\alpha_c = 0.43$), and they collapse for $\alpha < 0.43$.

with the minority opinion at the end is $\rho(\alpha, u_0) \approx u_0$. *For* $\alpha < \alpha_c(u_0)$ *consensus is slow, requiring* $O(N^2)$ *updates, and* $\rho(\alpha, u_0) \approx \rho(\alpha, 0.5)$.

Note that α_c is independent of u_0 in the rewire-to-same model. The behavior of the models for $\alpha > \alpha_c$ is easy to understand. As discussed above, when $\alpha = 1$ consensus will be reached in $O(N \log N)$ steps and when $\alpha = 0$ in $O(N^2)$ steps. Assume the boundary between the two dynamics takes N^τ $(1 < \tau < 2)$ steps to consensus on average. When an edge is chosen between voters with different opinions, then a rewiring event does not change the number of ones, whereas a voting event will increase and decrease the number of ones with equal probability. In other words, the number of ones $N_1(t)$ is a random walk:

$$N_1(t+1) = \begin{cases} N_1(t) & \text{with probability } \alpha \\ N_1(t)+1 & \text{with probability } \frac{1-\alpha}{2} \\ N_1(t)-1 & \text{with probability } \frac{1-\alpha}{2} \end{cases}$$

By Azuma's inequality:

$$P(|N_1(t) - N_1(0)| > x) \leq \exp(\frac{-x^2}{2t}),\ \forall\ x > 0.$$

Substituting in $x = \epsilon N$ and $t = N^\tau$, therefore

$$P(|\frac{N_1(t)}{N} - \frac{N_1(0)}{N}| > \epsilon) \leq \exp(\frac{-\epsilon N^{2-\tau}}{2}) \rightarrow 0, \text{as } N \rightarrow \infty.$$

The universal curve for $\alpha < \alpha_c$ is not trivial and will be examined in the following sections.

4.3. Quasi-Stationary Distributions

Considering one typical simulation of the rewire-to-random model, Figure 4.4 shows the changes over time of the fraction $N_1(t)/N$ of vertices with opinion 1 and the fraction $N_{01}(t)/M$ of discordant edges (i.e., edges connecting vertices with different opinions), starting from an Erdős-Rényi random graph with $N = 1000$ nodes and $M = 2000$ edges, and rewiring probability $\alpha = 0.3$. The initial density of ones is $u_0 \approx 0.3$, so the initial fraction of discordant 0-1 edges is approximately $2u_0(1 - u_0) = 0.42$, but the $N_{01}(t)/M$ curve drops very quickly to a value near 0.3, and then begins to change more slowly. The second key observation is that the fraction of 0-1 edges and the fraction of nodes with opinion 1 appear to be strongly correlated. The initial transient and the reason for the correlation will be seen more clearly in Figure 4.5.

Figure 4.5 shows results from simulations of the rewire-to-random model with rewiring probability $\alpha = 0.5$. The initial graph is Erdős-Rényi with $N = 100,000$ nodes and average degree $\lambda = 4$. Observations of the pair $(N_1(t)/N, N_{01}(t)/M)$ are plotted every 1,000 steps starting from densities $u_0 = 0.2$, 0.35, 0.5, 0.65, and 0.8. The plotted points converge quickly to a curve that is approximately (fitting to a parabola) $\approx 1.710x(1 - x) - 0.188$ and then diffuse along the curve until they hit the axis ($N_{01} = 0$) near 0.12 or 0.88. Thus the final fraction with the minority opinion $\rho \approx 0.12$, a value that agrees with the universal curve in Figure 4.1 (right) at $\alpha = 0.5$. This quadratic curve is fundamental

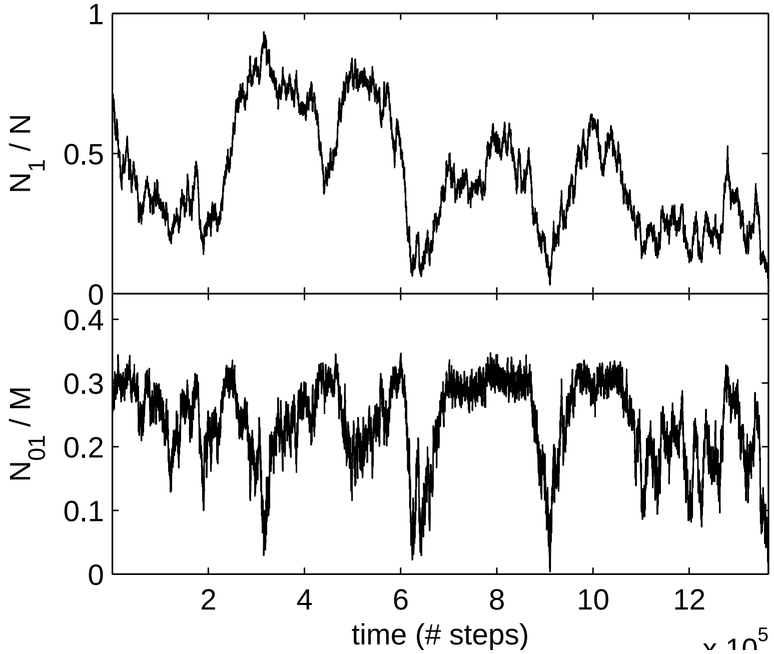

FIGURE 4.4. Time series of the fraction $N_1(t)/N$ of vertices with opinion 1 and the fraction $N_{01}(t)/M$ of discordant edges in one simulation, starting from an Erdős-Rényi random graph with $N = 1000$ nodes and $M = 2000$ edges, and rewiring probability $\alpha = 0.3$. The initial density of ones is $u_0 \approx 0.3$.

to the understanding of the observed system behavior, and it is referred to as the 'arch' hereafter.

The phenomena just described for $\alpha = 0.5$ also hold for other values of α. Figure 4.6 (right) shows the arches that correspond to $\alpha = 0.1, 0.2, ..., 0.7$ for the rewire-to-random model fitted from simulation data of $(N_1(t)/N, N_{01}(t)/M)$ as in Figure 4.5. Numerical results show that the curves are well approximated by $c_\alpha u(1-u) - b_\alpha$ for the rewire-to-random model. Let $(v(\alpha), 1-v(\alpha))$ be the "support interval" where the arch has positive values. Simulations show that if $u_0 < v(\alpha)$, then the simulated curve rapidly goes almost straight down and hits the axis where $N_{01} = 0$.

Though the nature of the phase transition looks different in the rewire-to-same model, the underlying picture is the same. Figure 4.6 (left) shows arches computed from simulations for the rewire-to-same model that correspond to the ones in the right panel of the figure for the rewire-to-random model. However, now all the arches have the same

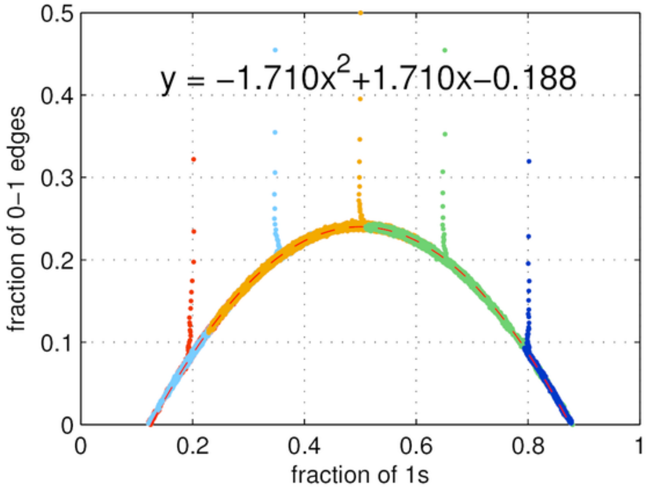

FIGURE 4.5. Evolution of the fraction of edges that are discordant 0-1 edges, $N_{01}(t)/M$, versus the population of opinion 1 $N_1(t)/N$ when $\alpha = 0.5$ for the rewire-to-random dynamic. Five simulations starting from u=0.2, 0.35, 0.5, 0.65, and 0.8 are plotted in different colors. Each simulation starts from an Erdős-Rényi graph with N=100,000 nodes and average degree $\lambda = 4$. After initial transients, the fraction of discordant edges behaves as a function of the population of opinions.

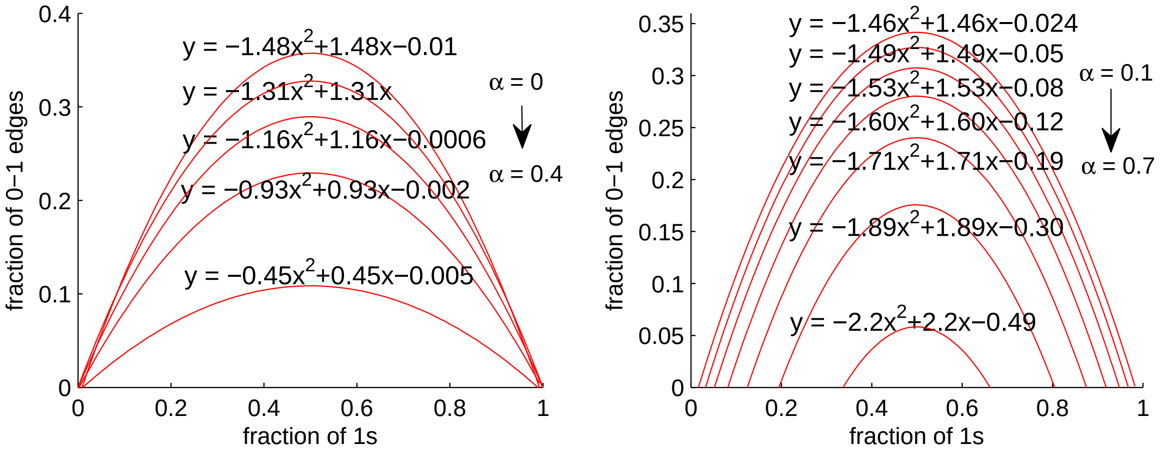

FIGURE 4.6. Observed arches for the rewire-to-same model (left) and the rewire-to-random model (right). The specified parabolas are fits to simulation data with $N = 10,000$ nodes and average degree $\lambda = 4$.

support interval, $(0, 1)$, and the formulas in the figure show that the curves are well approximated by $c_\alpha u(1 - u)$ for different values of α. Vazquez *et al.* [131] noticed similar behavior that the fraction of active links N_{01}/M plotted versus the fraction of ones converged rapidly to an arch and then diffused along it (figure 4 in [131]).

To explain the arches derived from simulations, recall results for the voter model on the d-dimensional integer lattice $\mathbb{Z}^d$, in which each node decides to change its opinion at rate 1, and when it does, it adopts the opinion of one of its $2d$ nearest neighbors chosen at random. Let $\xi_t(x)$ be the opinion of the voter at x at time t. Holley and Ligget [134] and Liggett [135] proved the following result.

Theorem 4.3.1. *[134, 135] In $d \leq 2$, the voter model approaches complete consensus; that is, if $x \neq y$ then $P[\xi_t(x) \neq \xi_t(y)] \to 0$. In $d \geq 3$, if the voter model starts from product measure with density p (i.e., $\xi_0^p(x)$ are independent and equal to one with probability p), then $\xi_t^p(x)$ converges in distribution to a limit ν_p, which is a stationary distribution for the voter model.*

Simulations of the voter model are done on a finite set, typically the torus ($\mathbb{Z}$ mod $L)^d$. In this setting, the behavior of the voter model is "trivial" because it is a finite Markov chain with two absorbing states, all ones and all zeros. As the next result shows (Cox and Greven [136]), the voter model has interesting behavior along the road to absorption.

Theorem 4.3.2. *[136] If the voter model on the torus in $d \geq 3$ starts from product measure with density p, then at time Nt it looks locally like $\nu_{\theta(t)}$ where the density $\theta(t)$ changes according to the Wright-Fisher diffusion process*

$$d\theta_t = \sqrt{\beta_d \cdot 2\theta_t(1-\theta_t)}dB_t$$

and β_d is the probability that two random walks starting from neighboring sites never hit.

The fact that, after the initial transient, $N_{01}(t)/M$ is a function of $N_1(t)/N$ suggests that the evolving voter model has a one parameter family of quasi-stationary distributions analogues to Cox and Greven [136]. To make it easier to compare the results here with the previous papers, time is rescaled so that times between updating steps are exponential with rate M, where M is the total number of edges. Let $v(\alpha) = \rho(\alpha, 0.5)$.

Two conjectures similar to Cox and Greven [136] are proposed for the two evolving voter models:

Conjecture 4.3.1. *In the rewire-to-random model, if* $\alpha < \alpha_c(1/2)$ *and* $v(\alpha) < u_0 \leq 1/2$ *then starting from product measure with density* u_0 *of 1's, the evolving voter model converges rapidly to a quasi-stationary distribution* ν_{α,u_0}*. At time* tM *the evolving voter model looks locally like* $\nu_{\alpha,\theta(t)}$ *where the density* $\theta(t)$ *changes according to a generalized Wright-Fisher diffusion process*

$$d\theta_t = \sqrt{(1-\alpha)[c_\alpha\theta_t(1-\theta_t) - b_\alpha]}dB_t \tag{4.2}$$

until θ_t *reaches* $v(\alpha)$ *or* $1 - v(\alpha)$*, the two solutions of* $c_\alpha x(1-x) = b_\alpha$*.*

Conjecture 4.3.2. *In the rewire-to-same model, the behavior is as described in Conjecture 4.3.1 but now* $b_\alpha = 0$*, so* α_c *is independent of the initial density* u_0*, and for* $\alpha < \alpha_c$*,* $\rho(\alpha, u_0) \approx 0$*.*

To begin to explain the behavior of θ_t given in (4.2), note that when an edge is picked with two endpoints that differ, a rewiring will not change the number of 1's, while a voting event, which occurs with probability $(1-\alpha)$, will result in an increase or decrease of the number of 1's with equal probability. Hence the quantity under the square root is $(1-\alpha)N_{01}/M$ with $(1-\alpha)$ equal to the fraction of steps that are voter steps because rewiring steps do not change the number of ones. When $\theta_t = u$ the rate at which 0-1 edges are chosen is equal to the expected fraction of 0-1 edges under $\nu_{\alpha,u}$, which is $c_\alpha u(1-u) - b_\alpha$.

4.4. Evolution of Network Statistics

If the above conjectures are true, then the values of all of the graph statistics can be computed from N_1/N. This is somewhat analogous to a stationary distribution from equilibrium statistical mechanics—e.g., the Maxwell-Boltzmann distribution associating the velocity distribution with the temperature. To further test this hypothesis, several network statistics are examined for the rewire-to-random model in this section. Results for the rewire-to-same model are similar.

4.4.1. Joint Distribution of the Opinions at Three Sites. Let N_{ijk} be the number of oriented triples x-y-z of adjacent nodes having opinions i, j, k, respectively. Note for example, in the $0-1-0$ case, this will count all such triples twice, but this is the approach taken in the theory of limits of dense graphs [137], where the general statistic is the number of homomorphisms of some small graph (labeled by ones and zeros in our case) into the random graph being studied.

Figure 4.7 shows four plots of $N_{ijk}(t)/N$ versus $N_1(t)/N$ for $\alpha = 0.5$ and $u_0 = 1/2$. After an initial transient, in each subplot the observed values stay close to a curve that is well approximated by a cubic polynomial. Because the numbers of $0-1-0$ triples must vanish when the number of $0-1$ edges do, the fitted cubic shares two roots with the quadratic approximating the graph of N_{01}/M versus N_1/N.

4.4.2. Degree Distribution. The degree of a node is its number of neighbors. The degree distribution of an Erdős-Rényi random graph with average degree λ is known to be $Poisson(\lambda)$. However, the degree distribution does not remain $Poisson(\lambda)$ throughout the process.

Figure 4.8 shows the degree distributions in the consensus state for five simulations starting at initial density of ones $u_0 = 0.1$, 0.2, 0.3, 0.4 and 0.5 respectively. The initial graphs are Erdős-Rényi random graphs with $N = 100,000$ nodes and average degree $\lambda = 4$. The probability density function of $Poisson(4)$ is shown for comparison. The rewiring probability is $\alpha = 0.6$ larger than $\alpha_c(0.1)$ but less than $\alpha_c(0.2)$. Hence the final degree distribution starting from $u_0 = 0.1$ is different from others. Regardless, Figure 4.8 indicates that the final degree distribution is close to but not *Poisson*; however, the final degree distribution does not depend on the initial density u_0 for $\alpha < \alpha_c(u_0)$. The skewness in the distributions may be due to the fragmentation of the network in the end.

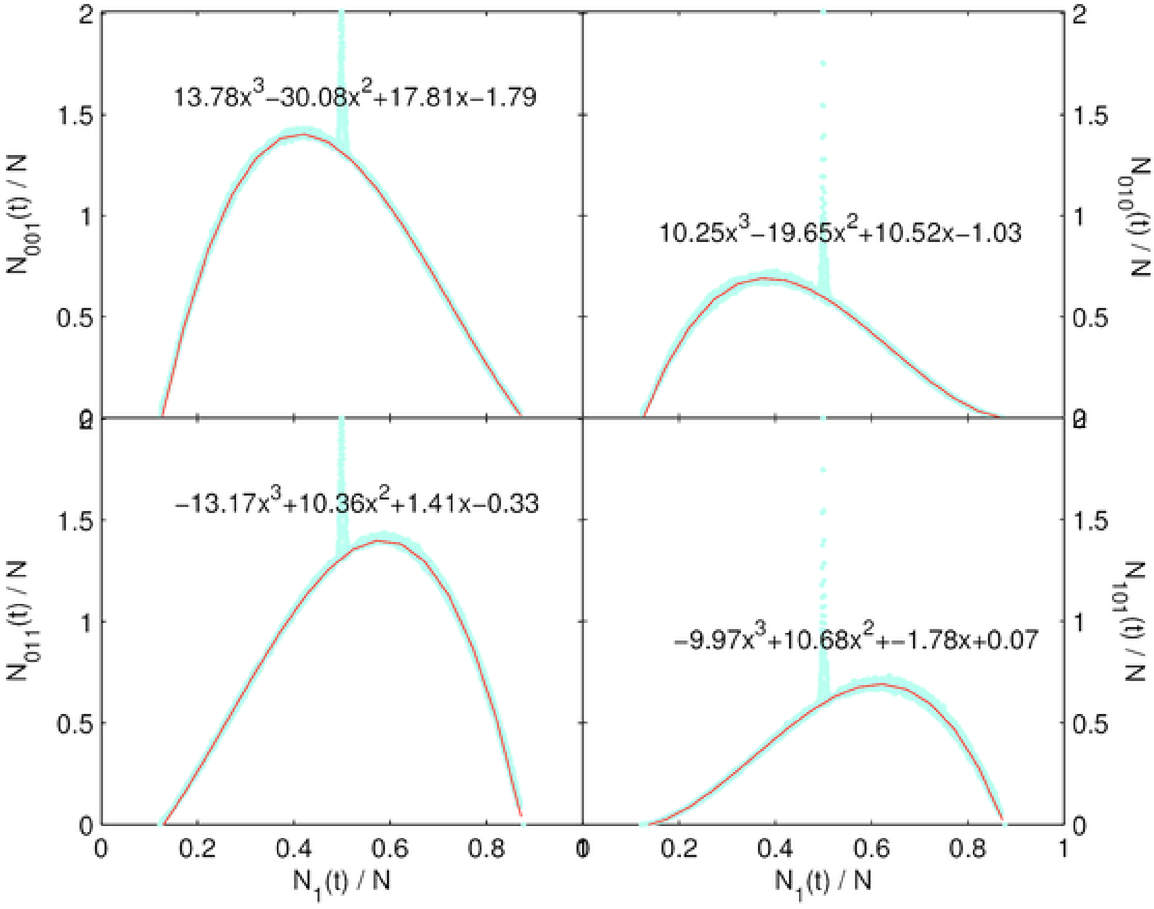

FIGURE 4.7. Evolution of the number of oriented triples $N_{ijk}(t)/N$ versus the population with opinion 1 $N_1(t)/N$, when $\alpha = 0.5$ for the rewire-to-random model. All simulations start at $u_0 = 0.5$ because multiple runs from one starting point are enough to explore all of the arch. Each simulation starts from an Erdős-Rényi graph with N=100,000 nodes and average degree $\lambda = 4$. After an initial transient, in each subplot the observed values stay close to a curve that is well approximated by a cubic polynomial.

Figure 4.9 (left) shows the changes in the average degrees of nodes with opinion 0, nodes with opinion 1 and all the nodes in the network, against the fraction $N_0(t)/N$ of nodes with opinion 0. Simulations start from Erdős-Rényi random graphs with $N = 10,000$ nodes and average degree $\lambda = 3$. The initial density of ones $u_0 = 0.5$ and the rewiring probability $\alpha = 0.3$. The average degree of the whole network remains the same simply because the number of nodes and the number of edges do not change during the process. The average degree of 1-nodes (i.e., nodes with opinion 1) depends linearly

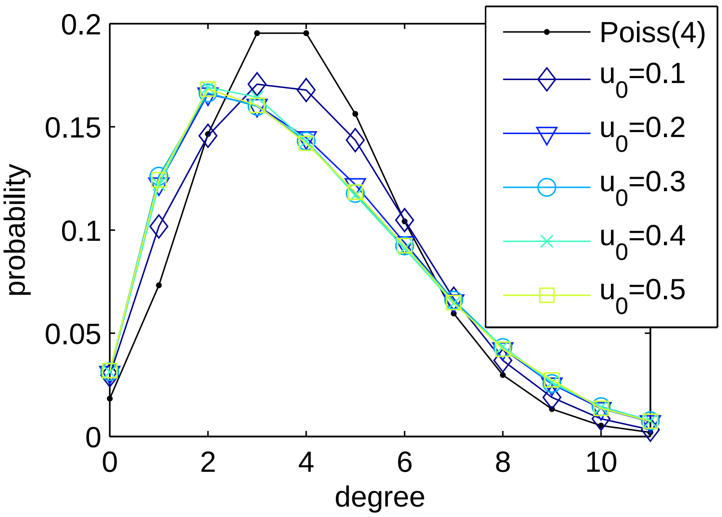

FIGURE 4.8. Degree distributions in the consensus state for five simulations starting at initial density of ones $u_0 = 0.1$, 0.2, 0.3, 0.4 and 0.5 respectively. The initial graphs are Erdős-Rényi random graphs with $N = 100,000$ nodes and average degree $\lambda = 4$. The probability density function of $Poisson(4)$ is shown for comparison. The rewiring probability is $\alpha = 0.6$ larger than $\alpha_c(0.1)$ but less than $\alpha_c(0.2)$. Hence the final degree distribution starting from $u_0 = 0.1$ is different from others.

on the inverse of the fraction of 1-nodes, and so does 0-nodes. To see this relationship clearer, Figure 4.9 (right) presents the same data in a slightly different way. Denoting the degree of a node v by $d(v)$ and the opinion of a node v by $\xi(v)$, the average degree of 1-nodes is calculated as

$$E[d(v)|\xi(v) = 1] = \frac{1}{N_1} \sum_{\xi(v)=1} d(v).$$

Instead, Figure 4.9 (right) plots $\sum_{\xi(v)=i} d(v)/N$ for i-nodes against the fraction of 0-nodes N_0/N. The straight lines indicate that $\sum_{\xi(v)=i} d(v)/N$ is a linear function of N_0/N, and hence $E[d(v)|\xi(v) = 0] = \sum_{\xi(v)=0} d(v)/N_0$ is a linear function of $1/N_0$. In other words, the number of "stubs" or edge ends in opinion i (i.e., $\sum_{\xi(v)=i} d(v)$) is linear in the fraction of nodes in opinion i. The two curves correspond to 0-nodes and 1-nodes cross at $N_0/N = 0.5$ because at that point the system is symmetric under interchange of 0's and 1's the the two classes of nodes will be statistically similar.

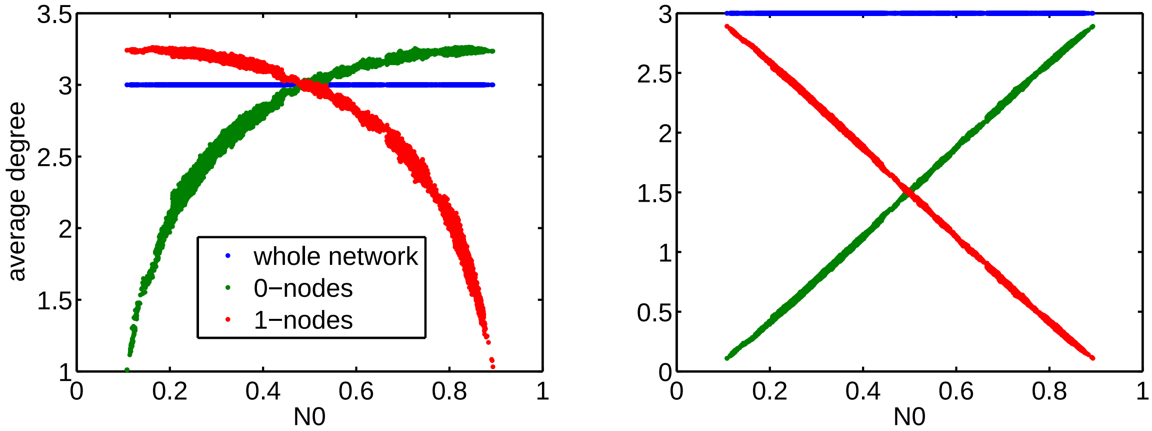

FIGURE 4.9. Left: changes in the average degrees of nodes with opinion 0, nodes with opinion 1 and all the nodes in the network, against the fraction $N_0(t)/N$ of nodes with opinion 0. Simulations start from Erdős-Rényi random graphs with $N = 10,000$ nodes and average degree $\lambda = 3$. The initial density of ones $u_0 = 0.5$ and the rewiring probability $\alpha = 0.3$. Right: the number of "stubs" or edge ends in opinion i (i.e., $\sum_{\xi(v)=i} d(v)$) normalized by the total number of nodes against the fraction of 0-nodes $N_0(t)/N$. The data shown are the same as in the left panel but presented differently.

One interesting observation from Figure 4.9 is that the average degree of the minority at the end is approximately 1. Combining with the linear dependence of $\sum_{\xi(v)=i} d(v)/N$ on N_i/N, this observation provides an alternative to calculate the population density at the end. Specifically, assume opinion 0 is the minority opinion at the end, and the linear relationship

$$\frac{1}{N}\sum_{\xi(v)=0} d(v) = a\frac{N_0}{N} + b.$$

Solving

$$1 = \frac{1}{N_0}\sum_{\xi(v)=0} d(v) = a + b\frac{N}{N_0},$$

yields

$$\rho = \frac{N_0}{N} = \frac{b}{1-a}.$$

4.5. Conclusion

This chapter discusses a model in which the opinions of individuals and network structure coevolve. Based on a combination of simulations and heuristic arguments it is concluded that (i) there is a discontinuous transition in the rewire-to-same model, similar to that in Holme and Newman [34], which occurs at an α_c independent of the initial fraction u_0 of ones; and (ii) there is a continuous transition in the rewire-to-random model at the critical value $\alpha_c(u_0)$ that depends on u_0, and the curves for the final fraction $\rho(\alpha, u_0)$ of voters in the minority agree with $\rho(\alpha, 0.5)$ for $\alpha < \alpha_c(u_0)$. Therefore a small change in the dynamics of the model results in a large change in the qualitative behavior. Moreover, in the rewire-to-same case, the size of the minority opinion shrinks to almost zero for $\alpha < \alpha_c$, whereas in the rewire-to-random case, the group fissions into two, leaving a significant minority group. Conjectures are made on a family of quasi-stationary distributions of the system, which explain the phase transitions and the qualitative difference in behaviors of the two models. However, it would be nice to derive results directly from the exact differential equations and in a way that gives some insight into the mechanisms underlying the differences between the two models.

CHAPTER 5

Multi-Opinion Evolving Voter Model

5.1. Introduction

Böhme and Gross [138] have studied the three-opinion version of the evolving voter model with rewire-to-same dynamics. In this case, the limiting behavior is complicated — one may have partial fragmentation (1's split off rapidly from the 2's and 3's) in addition to full fragmentation and coexistence of the three opinions. See their Figures 3–5. As seen in the present chapter, the behavior of the multi-opinion rewire-to-random model is much simpler because small groups of individuals with the same opinion will be drawn back into the giant component. This chapter aims to extend the understanding of the two-opinion model behavior to the same model with large numbers of opinions.

5.2. Multi-Opinion Model

Consider now the k-opinion (namely 1,2,...,k) model in which voters are assigned independent initial opinions that are equal to opinion i with probability u_i. In other words, u_i can be treated as the fraction of nodes with opinion i, and it will change as the system evolves. Let $u = (u_1, u_2, ..., u_k)$ and let $N_{\neq}$ be the number of edges at which the endpoint opinions differ. When $k = 3$, frequencies of the three types must lie in the triangle of possible values $\Delta = \{u = (u_1, u_2, u_3) : u_i \geq 0, \sum_i u_i = 1\}$. To preserve symmetry, Δ is drawn as an equilateral triangle in barycentric coordinates by mapping $(x, y, z) \to (x, z\sqrt{3}/2)$. The top panel in Figure 5.1 plots $N_{\neq}(t)/M$ as a function of the opinion densities as the system evolves, generalizing the one-dimensional arch observed for $k = 2$ to a two-dimensional cap for $k = 3$. Multiple simulations corresponding to different initial densities are shown while each one starts from an Erdős-Rényi graph with N=10,000 nodes and average degree $\lambda = 4$.

Generalizing the parabolic form of the arch for $k = 2$, the high-dimensional arch is conjectured to be

$$E_u N_{\neq}/M = \frac{c_2(\alpha)}{2}\left(1 - \sum_{i=1}^{k} u_i^2\right) - c_0(\alpha). \tag{5.1}$$

As in the two opinion case, the simulated values come quickly to the surface and then diffuse along it. In some situations, one opinion is lost before consensus occurs and the evolution reduces to that for the two opinion case. However, in one of the simulations shown, the realization ending with $x \approx 0.5$, all three opinions persist until the end.

The picture is somewhat easier to understand if looking at the cap from a top view, where the $E_u N_{\neq} = 0$ level sets for different α are observed to be circles. The bottom panel of Figure 5.1 plots the $E_u N_{\neq} = 0$ circles for different α's fitted from simulation data using Eq. (5.1) as well as the consensus opinion frequencies from the simulations (indicated by small circle data points). The two agree with each other up to small stochastic fluctuations. The size of the $E_u N_{\neq} = 0$ level set then dictates different consensus state properties. For example, the circle corresponding to $\alpha = 0.5$ intersects Δ in three disconnected arcs. As α increases, the radius of the $E_u N_{\neq} = 0$ level set decreases. When $\alpha > \alpha_c(1/2)$, the critical value of the two opinion model, the circle $E_u N_{\neq} = 0$ falls fully inside the triangle, so an initial condition including all three opinions will continue to demonstrate all three opinions at consensus. For example, the small circles around the innermost circle give the ending frequencies for several simulations for $\alpha = 0.8$. If the initial frequencies fall within the $E_u N_{\neq} = 0$ circle, then the model will quickly relax to the quasi-stationary distributions above the circle and then diffuse along the cap until consensus is reached at some $E_u N_{\neq} = 0$ point. If instead the initial frequencies u fall outside the $E_u N_{\neq} = 0$ circle—that is, for α above the phase transition point $\alpha_3(u)$—the consensus time jumps from $O(N^2)$ to $O(N \log N)$, similar to $\alpha_c(u)$ for the two-opinion model, with the final opinion frequencies essentially the same as the initial u. What is new in this case is that when starting with three opinions and $\alpha_c(u) < \alpha < \alpha_3(u) \leq \alpha_3(\{\frac{1}{3}, \frac{1}{3}, \frac{1}{3}\})$, the system always ends up with three distinct opinions.

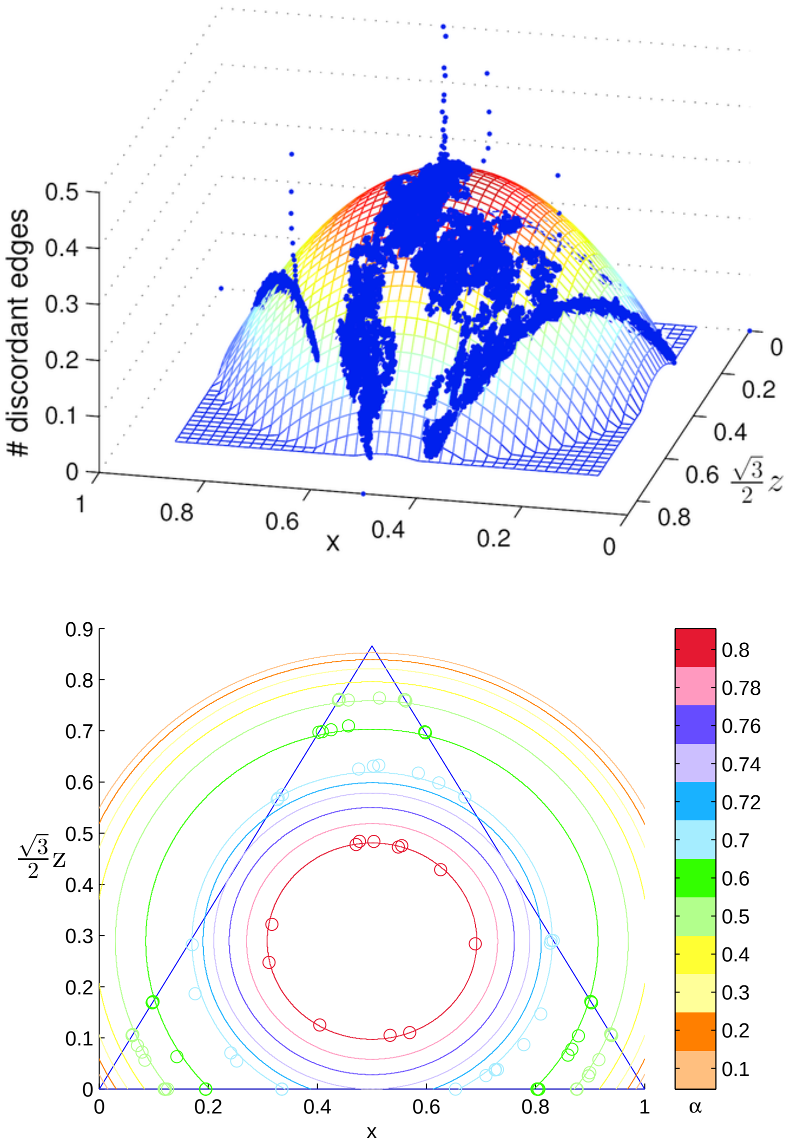

Figure 5.1. Top: plot of the fraction of discordant edges versus the population of opinions in barycentric coordinates for three opinions and $\alpha = 0.5$. Multiple simulations corresponding to different initial densities are shown while each one starts from an Erdős-Rényi graph with N=10,000 nodes and average degree $\lambda = 4$. Similar to the two-opinion case, the simulations quickly converge to a parabolic cap of quasi-stationary distributions. Bottom: top view of the parabolic caps of quasi-stationary distributions for α=0.1,0.2,...,0.8. The parabolic cap Eq. (5.1) are fitted to simulation data at various α's and then the level sets $E_u N_{\neq} = 0$ are plotted, which are the intersections of the parabolic caps with the $N_{\neq} = 0$ plane, as the large circles with colors indicating values of α.

For $k > 3$, simulation results indicate the same type of behavior as the system evolves. Define α_k to be the largest α for which consensus takes $O(N^2)$ updates when starting with k opinions with density $1/k$ for each opinion. Then as $k \to \infty$ the multi-opinion model has infinitely many phase transitions. When $\alpha_k < \alpha < \alpha_{k+1}$, consensus occurs after $O(N \log N)$ steps if the model starts with k opinions, while if starting with $k+1$ equally likely opinions the system quickly converges to a quasi-stationary distribution and diffuses until consensus occurs after $O(N^2)$ updates and there will always be $k+1$ opinions present at the end. The associated picture is the natural dimensional extension of the relationship between the $k = 2$ and $k = 3$ models: just as $\alpha_2 = \alpha_c(1/2)$ corresponds to the point at which the $E_u N_{\neq} = 0$ circle for $k = 3$ is the inscribed circle within the Δ triangle, α_3 corresponds to the point at which the $E_u N_{\neq} = 0$ circle reaches zero radius—that is, the point at which the $E_u N_{\neq} = 0$ sphere for $k = 4$ has become the inscribed sphere within the corresponding barycentric tetrahedron.

5.3. Quantitative Characterization of Quasi-Stationary Distributions

For each k, the multi-opinion rewire-to-random model is simulated starting from k opinions with each opinion taking $1/k$ fraction of nodes at random for a wide range of α's. Generalizing the picture of the one-dimensional arch for $k = 2$ and the two-dimensional cap for $k = 3$, the number of discordant edges as a function of opinion frequencies conjectured in Eq. (5.1) is a co-dimension 1 hypersurface characterizing the quasi-stationary states, and the behavior of the equal-initial-populations case allows to describe this surface, thereby characterizing behaviors for general initial populations.

The critical α_k's are identified when the slow diffusion of $N_{\neq}$ cannot be observed for the first time as α increases from 0 to 1. Then $N_{\neq}(t)/M$ is fitted to $u_i(t) = N_i(t)/N$ $(i = 1, ..., k)$ using Eq. (5.1) at every α up to α_k, and the fitted coefficients c_0 and c_2 are plotted against $\beta = \alpha/(1-\alpha)$ in Figure 5.2. Remarkably, the coefficients in Eq. (5.1) appear to be well approximated by linear functions of $\beta = \alpha/(1-\alpha)$. The graphs shows some curvature near $\beta = 0$, which may be caused by the fact that $\beta = 0$ $(\alpha = 0)$

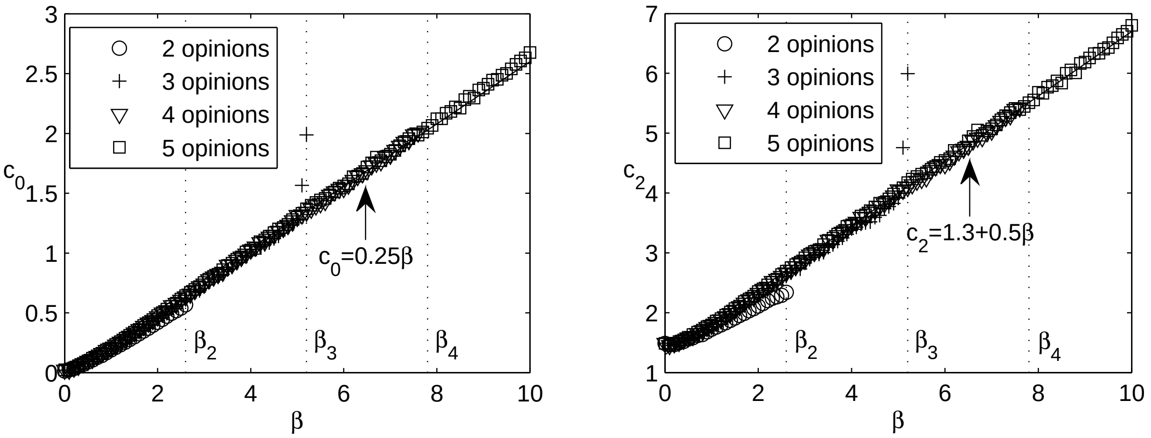

FIGURE 5.2. Coefficient $c_0(\beta)$ (left) and $c_2(\beta)$ (right) in Eq. (5.1) for models with multiple opinions. Each value of the coefficients is obtained by fitting Eq. (5.1) to multiple simulations starting from Erdős-Rényi graphs with N=100,000 nodes and average degree 4. The fitting error is very small ($R^2 \approx 0.99$) except for β close to the critical values.

corresponds to a voter model without evolution of the underlying network. The rest of the chapter will work with β for simplicity. Naturally, critical points α_k translate to $\beta_k = \alpha_k/(1-\alpha_k)$.

The fitted coefficients from the 2-opinion model deviate slightly from those fitted from higher-order models, which implies that Eq. (5.1) is not universal for the multi-opinion model and higher-order terms are possible. However, while the discrepancy between the fitted coefficients of the 2-opinion model and those of the 3-opinion one is apparent, difference between fitted coefficients of higher-order models is negligible, which implies that the inclusion of higher-order terms beyond the 3rd would not make significant changes to the equation. To probe the effect of higher-order terms we introduce terms up to kth order for k opinions. Noting $(\sum_i u_i)^2 = 1$, Eq. (5.1) is equivalent to:

$$E_u N_{\neq}/M = -c_0(\alpha) + c_2(\alpha) \sum_{i,j=1;i>j}^{k} u_i u_j. \tag{5.2}$$

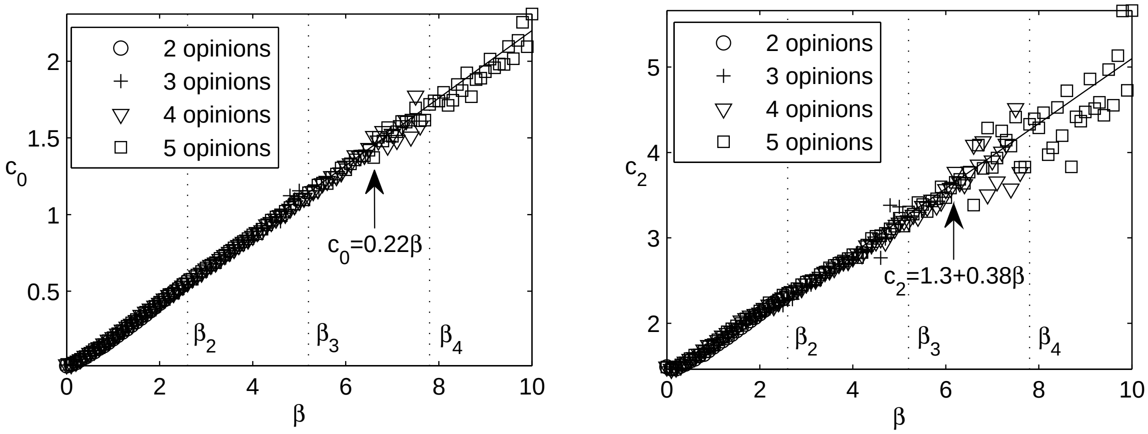

FIGURE 5.3. Coefficients $c_0(\beta)$ (left) and $c_2(\beta)$ (right) in Eq. (5.3) for models with multiple opinions. Each value of the coefficients is obtained by fitting Eq. (5.3) to the same data as in Figure 5.2.

Given the symmetry of the system in u_i's, the only possible choice in degree-k polynomials is:

$$\begin{aligned} E_u N_{\neq}/M \;=\; & -c_0(\alpha) + c_2(\alpha) \sum_{\{i_1,i_2\}\in\mathcal{A}_2} u_{i_1}u_{i_2} \\ & + c_3(\alpha) \sum_{\{i_1,i_2,i_3\}\in\mathcal{A}_3} u_{i_1}u_{i_2}u_{i_3} + \cdots \\ & + c_k(\alpha) \sum_{\{i_1,\cdots,i_k\}\in\mathcal{A}_k} u_{i_1}u_{i_2}\cdots u_{i_k}, \end{aligned} \tag{5.3}$$

where $\mathcal{A}_i$ is the collection of all i-element subsets of $\{1, 2, ..., k\}$. Using the same simulation data as above, $N_{\neq}(t)/M$ is refitted to $u_i(t)$'s ($i = 1, ..., k$) according to the generalized formula Eq. (5.3) and the fitted coefficients c_0 and c_2 are plotted against β in Figure 5.3. Fitting diagnostics suggest that higher-order terms are significant from zero (with p-values $< 10^{-4}$) and it can be seen that those terms explain the inconsistency between fitted coefficients of different models in Figures 5.2. However, the difference between the two fitted functions of Eq. (5.1) and Eq. (5.3) is actually small ($\approx .1$ in L^2-norm) and thus higher-order terms are small corrections to the hyper-surface Eq. (5.1).

Values of the coefficients $c_i(\beta)$ for the three opinion model near its critical value $\beta_3 \approx 5.2$ show some scatter, but this is to be expected since the surface is very small at this point. Values for the four opinion model appear to become more difficult to fit prior to β_4 since $E_u N_{\neq} = 0$ is a three-dimensional hyper-surface in four-dimensional space, so much more data is required to get reliable estimates of coefficients.

As is visually apparent in Figure 5.3, the coefficients c_0 and c_2 for the first two terms in Eq. (5.3) are well approximated by linear functions, with best fits $c_0(\beta) \approx 0.22\beta$ and $c_2(\beta) \approx 1.3 + 0.38\beta$, while coefficients for higher-order terms are not linear in β (e.g., see Figure 5.4 for $c_3(\beta)$). For comparison, the best fits for c_0 and c_2 in Eq. (5.1) (as in Figure 5.2) are

$$c_2(\beta) \approx 1.3 + 0.5\beta, \qquad c_0(\beta) \approx 0.25\beta. \tag{5.4}$$

Since Eq. (5.1) well approximate the higher-order hyper-surface Eq. (5.3), its simple form can be used to estimate the critical points for phase transitions. Combining (5.1) and (5.4), and then solving

$$(0.65 + 0.25\beta)(1 - k(1/k)^2) - 0.25\beta = 0$$

gives

$$\beta_k = 2.6(k-1)\,.$$

which agrees with the critical β_k's identified when the slow diffusion of $N_{\neq}$ cannot be observed in simulations as β increases.

5.4. Conclusion

The multi-opinion voter model studied here has infinitely many phase transitions. When $\beta_k < \beta < \beta_{k+1}$, freezing occurs rapidly when we start with k opinions; however, starting with $k+1$ equally likely opinions will always yield $k+1$ opinions present at freezing for this β range (Figure 5.5). A corollary drawn from Figure 5.5 is that when starting from $n > k+1$ opinions and $\beta_k < \beta < \beta_{k+1}$, the number of different opinions at the end can be any number between $k+1$ and n, and its distribution deserves further study. To a good approximation $\beta_k = 2.6(k-1)$, but the departures from linearity in

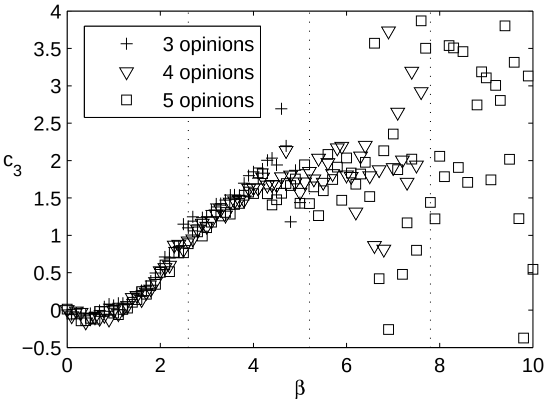

FIGURE 5.4. Coefficient $c_3(\beta)$ in Eq. (5.3) for models with multiple opinions. Each value of $c_3(\beta)$ is obtained by fitting Eq. (5.3) to the same data in Figure 5.2.

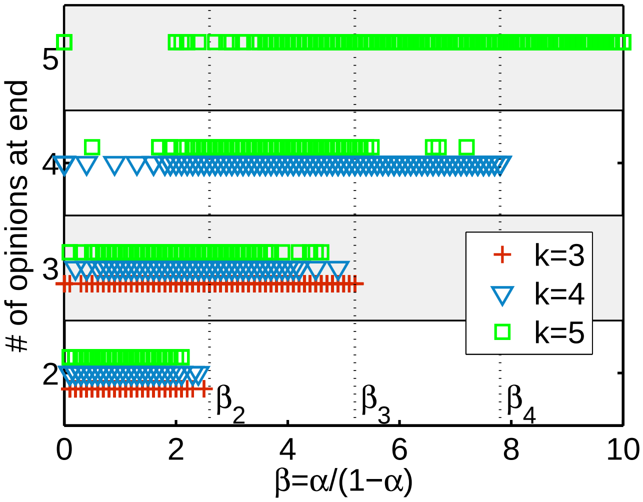

FIGURE 5.5. Number of opinions observed at freezing for different $\beta = \alpha/(1-\alpha)$, starting from k equally likely opinions. Each data point corresponds to a simulation starting from an Erdős-Rényi graph with 100,000 nodes and average degree 4. Results above β_k when starting from k opinions are omitted because the final density of opinions under such conditions is the same as the initial density.

the plots of $c_2(\beta)$ and $c_0(\beta)$ suggest that this result is not exact. However, formulas for various quantities associated with this model are close to polynomials, so an exact solution may be possible.

More complicated rewiring rules might also be considered, particularly if they maintained high clustering or other global macroscopic properties. An even more complete understanding of the present rewiring system would help motivate similar investigations for other rewiring rules.

References

[1] D. Stauffer, J. Adler, and A. Aharony, “Universality at the three-dimensional percolation threshold,” *Journal of Physics A: Mathematical and General*, vol. 27, no. 13, p. L475, 1999.

[2] X. Zheng, M. Forest, R. Vaia, M. Arlen, and R. Zhou, “A strategy for dimensional percolation in sheared nanorod dispersions,” *Advanced Materials*, vol. 19, no. 22, pp. 4038–4043, 2007.

[3] F. C. MacKintosh, J. Käs, and P. A. Janmey, “Elasticity of semiflexible biopolymer networks,” *Physical Review Letters*, vol. 75, p. 4425, Dec. 1995.

[4] D. J. Watts and S. H. Strogatz, “Collective dynamics of ‘small-world’ networks,” *Nature*, vol. 393, pp. 440–442, June 1998.

[5] A.-L. Barabási and R. Albert, “Emergence of scaling in random networks,” *Science*, vol. 286, pp. 509–512, Oct. 1999.

[6] D. S. Callaway, M. E. J. Newman, S. H. Strogatz, and D. J. Watts, “Network robustness and fragility: Percolation on random graphs,” *Physical Review Letters*, vol. 85, p. 5468, Dec. 2000.

[7] M. E. J. Newman, “Spread of epidemic disease on networks,” *Physical Review E*, vol. 66, p. 016128, July 2002.

[8] R. Albert and A.-L. Barabási, “Statistical mechanics of complex networks,” *Reviews of Modern Physics*, vol. 74, pp. 47–97, Jan. 2002.

[9] J. Wilhelm and E. Frey, “Elasticity of stiff polymer networks,” *Physical Review Letters*, vol. 91, no. 10, p. 108103, 2003.

[10] M. E. J. Newman, “The structure and function of complex networks,” *SIAM Review*, vol. 45, pp. 167–256, June 2003.

[11] S. Boccaletti, V. Latora, Y. Moreno, M. Chavez, and D.-U. Hwang, “Complex networks: Structure and dynamics,” *Physics Reports*, vol. 424, pp. 175–308, Feb. 2006.

[12] S. N. Dorogovtsev, A. V. Goltsev, and J. F. F. Mendes, “Critical phenomena in complex networks,” *Reviews of Modern Physics*, vol. 80, pp. 1275–1335, Oct. 2008.

[13] R. Pastor-Satorras and A. Vespignani, “Epidemics and immunization in scale-free networks,” *arXiv:cond-mat/0205260*, May 2002. Contribution to ”Handbook of Graphs and Networks: From the Genome to the Internet” eds. S. Bornholdt and H.G. Schuster (Wiley-VCH, Berlin, 2002).

[14] L. Sander, C. Warren, I. Sokolov, C. Simon, and J. Koopman, "Percolation on heterogeneous networks as a model for epidemics," *Mathematical Biosciences*, vol. 180, pp. 293–305, Nov. 2002.

[15] R. Cohen, S. Havlin, and D. ben Avraham, "Efficient immunization strategies for computer networks and populations," *Physical Review Letters*, vol. 91, p. 247901, Dec. 2003.

[16] M. Kretzschmar, V. Duynhoven, Y. T. H. P, and A. J. Severijnen, "Modeling prevention strategies for gonorrhea and chlamydia using stochastic network simulations," *American Journal of Epidemiology*, vol. 144, pp. 306–317, Aug. 1996.

[17] C. Storm, J. J. Pastore, F. C. MacKintosh, T. C. Lubensky, and P. A. Janmey, "Nonlinear elasticity in biological gels," *Nature*, vol. 435, pp. 191–194, May 2005.

[18] W. Willinger, D. Alderson, J. C. Doyle, and N. P. S. M. CA, *Mathematics and the internet: A source of enormous confusion and great potential.* Defense Technical Information Center, 2009.

[19] M. Granovetter, "Threshold models of collective behavior," *American Journal of Sociology*, vol. 83, pp. 1420–1443, May 1978.

[20] "The DIMES project."

[21] K. Venkatesan, J.-F. Rual, A. Vazquez, U. Stelzl, I. Lemmens, T. Hirozane-Kishikawa, T. Hao, M. Zenkner, X. Xin, K.-I. Goh, M. A. Yildirim, N. Simonis, K. Heinzmann, F. Gebreab, J. M. Sahalie, S. Cevik, C. Simon, A.-S. de Smet, E. Dann, A. Smolyar, A. Vinayagam, H. Yu, D. Szeto, H. Borick, A. Dricot, N. Klitgord, R. R. Murray, C. Lin, M. Lalowski, J. Timm, K. Rau, C. Boone, P. Braun, M. E. Cusick, F. P. Roth, D. E. Hill, J. Tavernier, E. E. Wanker, A.-L. Barabasi, and M. Vidal, "An empirical framework for binary interactome mapping," *Nat Meth*, vol. 6, pp. 83–90, Jan. 2009.

[22] O. Sporns, G. Tononi, and R. Ktter, "The human connectome: A structural description of the human brain," *PLoS Comput Biol*, vol. 1, p. e42, Sept. 2005.

[23] S. N. Dorogovtsev and J. F. F. Mendes, "Evolution of networks," *Advances in Physics*, vol. 51, no. 4, pp. 1079–1187, 2002.

[24] M. Newman, A.-L. Barabási, and D. J. Watts, *The Structure and Dynamics of Networks:*. Princeton University Press, 1 ed., Apr. 2006.

[25] G. Caldarelli, *Scale-Free Networks: Complex Webs in Nature and Technology.* Oxford University Press, USA, June 2007.

[26] R. Cohen and S. Havlin, *Complex Networks: Structure, Robustness and Function.* Cambridge University Press, Aug. 2010.

[27] A. Barrat, M. Barthélemy, and A. Vespignani, *Dynamical Processes on Complex Networks.* Cambridge University Press, Nov. 2012.

[28] B. Skyrms and R. Pemantle, "A dynamic model of social network formation," *Proceedings of the National Academy of Sciences*, vol. 97, pp. 9340–9346, Aug. 2000.

[29] T. Gross and B. Blasius, "Adaptive coevolutionary networks: A review," *Journal of The Royal Society Interface*, vol. 5, pp. 259–271, Mar. 2008.

[30] F. Shi, S. Wang, P. J. Mucha, and M. G. Forest, "Universal supercritical current distributions in 3D random resistor networks," *arXiv:1209.2483*, Sept. 2012.

[31] F. Shi, S. Wang, J. P. Much, G. Forest, X. Zheng, and R. Zhou, "Network analysis of anisotropic electrical properties in percolating sheared nanorod dispersions," *submitted*, 2012.

[32] R. Durrett, J. P. Gleeson, A. L. Lloyd, P. J. Mucha, F. Shi, D. Sivakoff, J. E. S. Socolar, and C. Varghese, "Graph fission in an evolving voter model," *Proceedings of the National Academy of Sciences*, vol. 109, pp. 3682–3687, Mar. 2012.

[33] F. Shi, P. J. Mucha, and R. Durrett, "A multi-opinion evolving voter model with infinitely many phase transitions," *arXiv:1303.7434*, Mar. 2013.

[34] P. Holme and M. E. J. Newman, "Nonequilibrium phase transition in the coevolution of networks and opinions," *Physical Review E*, vol. 74, p. 056108, Nov. 2006.

[35] S. R. Broadbent and J. M. Hammersley, "Percolation processes," *Mathematical Proceedings of the Cambridge Philosophical Society*, vol. 53, no. 03, pp. 629–641, 1957.

[36] H. Kesten, *Percolation Theory for Mathematics.* Birkhuser Boston, 1 ed., Nov. 1982.

[37] Wikipedia, "Percolation threshold," 2013.

[38] G. Deutscher, R. Zallen, and J. Adler, *Percolation structures and processes.* A. Hilger, 1983.

[39] D. Stauffer and A. Aharony, *Introduction to percolation theory.* CRC Press, 1994.

[40] G. R. Grimmett, *Percolation.* Springer, 2nd ed., June 1999.

[41] L. de Arcangelis, S. Redner, and A. Coniglio, "Anomalous voltage distribution of random resistor networks and a new model for the backbone at the percolation threshold," *Physical Review B*, vol. 31, no. 7, p. 4725, 1985.

[42] L. de Arcangelis, S. Redner, and A. Coniglio, “Multiscaling approach in random resistor and random superconducting networks,” *Physical Review B*, vol. 34, p. 4656, Oct. 1986.

[43] B. Lin, Z.-Z. Zhang, and B. Hu, “Multifractal characterization of random resistor and random superconductor networks,” *Physical Review A*, vol. 44, p. 960, July 1991.

[44] J. P. Straley, “Current distribution in random resistor networks,” *Physical Review B*, vol. 39, p. 4531, Mar. 1989.

[45] E. Duering, R. Blumenfeld, D. J. Bergman, A. Aharony, and M. Murat, “Current distributions in a two-dimensional random-resistor network,” *Journal of Statistical Physics*, vol. 67, pp. 113–121, Apr. 1992.

[46] E. Duering and D. J. Bergman, “Current distribution on a three-dimensional, bond-diluted, random-resistor network at the percolation threshold,” *Journal of Statistical Physics*, vol. 60, pp. 363–381, Aug. 1990.

[47] R. Rammal, C. Tannous, P. Breton, and A. M. S. Tremblay, “Flicker (1/f) noise in percolation networks: A new hierarchy of exponents,” *Physical Review Letters*, vol. 54, p. 1718?721, Apr. 1985.

[48] C.-W. Nan, Y. Shen, and J. Ma, “Physical properties of composites near percolation,” *Annual Review of Materials Research*, vol. 40, pp. 131–151, June 2010.

[49] G. G. Batrouni and A. Hansen, “Fracture in three-dimensional fuse networks,” *Physical Review Letters*, vol. 80, pp. 325–328, Jan. 1998.

[50] L. de Arcangelis, S. Redner, and H. Herrmann, “A random fuse model for breaking processes,” *Journal de Physique Lettres*, vol. 46, no. 13, pp. 585–590, 1985.

[51] P. M. Duxbury, P. L. Leath, and P. D. Beale, “Breakdown properties of quenched random systems: The random-fuse network,” *Physical Review B*, vol. 36, pp. 367–380, July 1987.

[52] B. Kahng, G. Batrouni, S. Redner, L. de Arcangelis, and H. Herrmann, “Electrical breakdown in a fuse network with random, continuously distributed breaking strengths,” *Physical Review B*, vol. 37, pp. 7625–7637, May 1988.

[53] S.-k. Chan, J. Machta, and R. A. Guyer, “Large currents in random resistor networks,” *Physical Review B*, vol. 39, pp. 9236–9239, May 1989.

[54] Y. S. Li and P. M. Duxbury, “Size and location of the largest current in a random resistor network,” *Physical Review B*, vol. 36, p. 5411, Oct. 1987.

[55] B. Kahng, G. Batrouni, and S. Redner, “Logarithmic voltage anomalies in random resistor networks,” *Journal of Physics A: Mathematical and General*, vol. 20,

p. L827, 1987.

[56] J. Machta and R. A. Guyer, “Largest current in a random resistor network,” *Physical Review B*, vol. 36, no. 4, p. 2142, 1987.

[57] C. D. Lorenz and R. M. Ziff, “Precise determination of the bond percolation thresholds and finite-size scaling corrections for the sc, fcc, and bcc lattices,” *Physical Review E*, vol. 57, p. 230?36, Jan. 1998.

[58] D. E. Knuth, *Art of Computer Programming, Volume 1: Fundamental Algorithms.* Addison-Wesley Professional, 3 ed., July 1997.

[59] G. Strang, *Introduction to Applied Mathematics.* Wellesley-Cambridge Press, Jan. 1986.

[60] E. J. Gumbel, *Statistics of Extremes.* Dover Publications, July 2004.

[61] C. Veerman, L. M. C. Sagis, P. Venema, and E. v. d. Linden, “The effect of shear flow on the percolation concentration of fibrillar protein assemblies,” *Journal of Rheology*, vol. 49, no. 2, pp. 355–368, 2005.

[62] S. B. Kharchenko, J. F. Douglas, J. Obrzut, E. A. Grulke, and K. B. Migler, “Flow-induced properties of nanotube-filled polymer materials,” *Nature Materials*, vol. 3, pp. 564–568, Aug. 2004.

[63] J. Xu, W. Florkowski, R. Gerhardt, K.-s. Moon, and C.-P. Wong, “Shear modulated percolation in carbon nanotube composites,” *The Journal of Physical Chemistry B*, vol. 110, pp. 12289–12292, June 2006.

[64] J. Obrzut, J. F. Douglas, S. B. Kharchenko, and K. B. Migler, “Shear-induced conductor-insulator transition in melt-mixed polypropylene-carbon nanotube dispersions,” *Physical Review B*, vol. 76, p. 195420, Nov. 2007.

[65] I. Balberg and N. Binenbaum, “Computer study of the percolation threshold in a two-dimensional anisotropic system of conducting sticks,” *Physical Review B*, vol. 28, p. 3799, Oct. 1983.

[66] I. Balberg, “Excluded-volume explanation of archie’s law,” *Physical Review B*, vol. 33, p. 3618, Mar. 1986.

[67] I. Balberg, C. H. Anderson, S. Alexander, and N. Wagner, “Excluded volume and its relation to the onset of percolation,” *Physical Review B*, vol. 30, p. 3933, Oct. 1984.

[68] I. Balberg, N. Binenbaum, and N. Wagner, “Percolation thresholds in the three-dimensional sticks system,” *Physical Review Letters*, vol. 52, p. 1465, Apr. 1984.

[69] A. L. R. Bug, S. A. Safran, and I. Webman, "Continuum percolation of rods," *Physical Review Letters*, vol. 54, p. 1412, Apr. 1985.

[70] S. H. Munson-McGee, "Estimation of the critical concentration in an anisotropic percolation network," *Physical Review B*, vol. 43, p. 3331, Feb. 1991.

[71] M. Grujicic, G. Cao, and W. N. Roy, "A computational analysis of the percolation threshold and the electrical conductivity of carbon nanotubes filled polymeric materials," *Journal of Materials Science*, vol. 39, pp. 4441–4449, July 2004.

[72] W. Bauhofer, S. Schulz, A. Eken, T. Skipa, D. Lellinger, I. Alig, E. Tozzi, and D. Klingenberg, "Shear-controlled electrical conductivity of carbon nanotubes networks suspended in low and high molecular weight liquids," *Polymer*, vol. 51, pp. 5024–5027, Oct. 2010.

[73] M. G. Forest, Q. Wang, and R. Zhou, "The flow-phase diagram of doi-hess theory for sheared nematic polymers II: finite shear rates," *Rheologica Acta*, vol. 44, pp. 80–93, July 2004.

[74] M. G. Forest, Q. Wang, and R. Zhou, "The weak shear kinetic phase diagram for nematic polymers," *Rheologica Acta*, vol. 43, pp. 17–37, Feb. 2004.

[75] M. Doi, "Molecular dynamics and rheological properties of concentrated solutions of rodlike polymers in isotropic and liquid crystalline phases," *Journal of Polymer Science: Polymer Physics Edition*, vol. 19, no. 2, 1981.

[76] S. Hess, "Fokker-planck-equation approach to flow alignment in liquid crystals," *Zeitschrift Naturforschung Teil A*, vol. 31, p. 1034, Sept. 1976.

[77] G. W. Milton, *The theory of composites.* Cambridge University Press, May 2002.

[78] X. Zheng, M. G. Forest, R. Lipton, R. Zhou, and Q. Wang, "Exact scaling laws for electrical conductivity properties of nematic polymer nanocomposite monodomains," *Advanced Functional Materials*, vol. 15, pp. 627–638, Apr. 2005.

[79] M. G. Forest, X. Zheng, R. Zhou, Q. Wang, and R. Lipton, "Anisotropy and dynamic ranges in effective properties of sheared nematic polymer nanocomposites," *Advanced Functional Materials*, vol. 15, pp. 2029–2035, Dec. 2005.

[80] R. H. Schmidt, I. A. Kinloch, A. N. Burgess, and A. H. Windle, "The effect of aggregation on the electrical conductivity of spin-coated Polymer/Carbon nanotube composite films," *Langmuir*, vol. 23, pp. 5707–5712, May 2007.

[81] T. Skipa, D. Lellinger, W. Bhm, M. Saphiannikova, and I. Alig, "Influence of shear deformation on carbon nanotube networks in polycarbonate melts: Interplay between build-up and destruction of agglomerates," *Polymer*, vol. 51, pp. 201–210, Jan. 2010.

[82] G. Kwon, Y. Heo, K. Shin, and B. J. Sung, “Electrical percolation networks of carbon nanotubes in a shear flow,” *Physical Review E*, vol. 85, p. 011143, Jan. 2012.

[83] Z. Ounaies, C. Park, K. E. Wise, E. J. Siochi, and J. S. Harrison, “Electrical properties of single wall carbon nanotube reinforced polyimide composites,” *Composites Science and Technology*, vol. 63, pp. 1637–1646, Aug. 2003.

[84] H.-P. Xu and Z.-M. Dang, “Electrical property and microstructure analysis of poly(vinylidene fluoride)-based composites with different conducting fillers,” *Chemical Physics Letters*, vol. 438, pp. 196–202, Apr. 2007.

[85] A. A. Gusev and M. G. Rozman, “Numerical search for morphologies providing ultra high elastic stiffness in filled rubbers,” *Computational and Theoretical Polymer Science*, vol. 9, pp. 335–337, Dec. 1999.

[86] A. A. Gusev and H. R. Lusti, “Rational design of nanocomposites for barrier applications,” *Advanced Materials*, vol. 13, no. 21, p. 1641?643, 2001.

[87] G. A. Buxton and A. C. Balazs, “Predicting the mechanical and electrical properties of nanocomposites formed from polymer blends and nanorods,” *Molecular Simulation*, vol. 30, no. 4, p. 249, 2004.

[88] R. Simoes, J. Silva, R. Vaia, V. Sencadas, P. Costa, J. Gomes, and S. Lanceros-Mendez, “Low percolation transitions in carbon nanotube networks dispersed in a polymer matrix: dielectric properties, simulations and experiments,” *Nanotechnology*, vol. 20, no. 3, p. 035703, 2009.

[89] J. Silva, R. Simoes, S. Lanceros-Mendez, and R. Vaia, “Applying complex network theory to the understanding of high-aspect-ratio carbon-filled composites,” *EPL (Europhysics Letters)*, vol. 93, p. 37005, Feb. 2011.

[90] G. B. Jeffery, “The motion of ellipsoidal particles immersed in a viscous fluid,” *Proceedings of the Royal Society of London. Series A, Containing Papers of a Mathematical and Physical Character*, vol. 102, pp. 161–179, Nov. 1922.

[91] G. I. Taylor, “The motion of ellipsoidal particles in a viscous fluid,” *Proceedings of the Royal Society of London. Series A, Containing Papers of a Mathematical and Physical Character*, vol. 103, pp. 58–61, Apr. 1923.

[92] R. C. Binder, “The motion of cylindrical particles in viscous flow,” *Journal of Applied Physics*, vol. 10, pp. 711–713, Oct. 1939.

[93] P. G. Saffman, “On the motion of small spheroidal particles in a viscous liquid,” *Journal of Fluid Mechanics*, vol. 1, no. 05, pp. 540–553, 1956.

[94] J. Feng and D. D. Joseph, “The unsteady motion of solid bodies in creeping flows,” *Journal of Fluid Mechanics*, vol. 303, no. -1, 1995.

[95] S. G. Mason and R. S. J. Manley, "Particle motions in sheared suspensions: Orientations and interactions of rigid rods," *Proceedings of the Royal Society of London. Series A. Mathematical and Physical Sciences*, vol. 238, pp. 117–131, Dec. 1956.

[96] L. G. Leal and E. J. Hinch, "The effect of weak brownian rotations on particles in shear flow," *Journal of Fluid Mechanics Digital Archive*, vol. 46, no. 04, pp. 685–703, 1971.

[97] E. J. Hinch and L. G. Leal, "The effect of brownian motion on the rheological properties of a suspension of non-spherical particles," *Journal of Fluid Mechanics Digital Archive*, vol. 52, no. 04, pp. 683–712, 1972.

[98] E. Volz, "SIR dynamics in random networks with heterogeneous connectivity," *Journal of Mathematical Biology*, vol. 56, pp. 293–310, Mar. 2008.

[99] J. C. Miller, "A note on a paper by erik volz: SIR dynamics in random networks," *Journal of Mathematical Biology*, vol. 62, pp. 349–358, Mar. 2011.

[100] M. Newman, *Networks: An Introduction.* Oxford University Press, USA, 1 ed., May 2010.

[101] V. Sood and S. Redner, "Voter model on heterogeneous graphs," *Physical Review Letters*, vol. 94, p. 178701, May 2005.

[102] R. Durrett, *Random Graph Dynamics.* Cambridge University Press, 1 ed., May 2010.

[103] C. Castellano, S. Fortunato, and V. Loreto, "Statistical physics of social dynamics," *Reviews of Modern Physics*, vol. 81, pp. 591–646, May 2009.

[104] D. J. Watts, "A simple model of global cascades on random networks," *Proceedings of the National Academy of Sciences of the United States of America*, vol. 99, pp. 5766–5771, Apr. 2002. PMID: 16578874 PMCID: 122850.

[105] J. P. Gleeson and D. J. Cahalane, "Seed size strongly affects cascades on random networks," *Physical Review E*, vol. 75, p. 056103, May 2007.

[106] A. Montanari and A. Saberi, "The spread of innovations in social networks," *Proceedings of the National Academy of Sciences*, Nov. 2010.

[107] H. Ohtsuki, C. Hauert, E. Lieberman, and M. A. Nowak, "A simple rule for the evolution of cooperation on graphs and social networks," *Nature*, vol. 441, pp. 502–505, May 2006.

[108] D. Easley and J. Kleinberg, *Networks, Crowds, and Markets: Reasoning About a Highly Connected World.* Cambridge University Press, July 2010.

[109] T. Gross and H. Sayama, eds., *Adaptive Networks: Theory, Models and Applications*. Springer, 2009 ed., Aug. 2009.

[110] H. Ebel and S. Bornholdt, "Coevolutionary games on networks," *Physical Review E*, vol. 66, p. 056118, Nov. 2002.

[111] M. G. Zimmermann, V. M. Eguluz, and M. San Miguel, "Coevolution of dynamical states and interactions in dynamic networks," *Physical Review E*, vol. 69, p. 065102, June 2004.

[112] M. Zimmermann and V. Eguluz, "Cooperation, social networks, and the emergence of leadership in a prisoners dilemma with adaptive local interactions," *Physical Review E*, vol. 72, Nov. 2005.

[113] F. C. Santos, J. M. Pacheco, and T. Lenaerts, "Cooperation prevails when individuals adjust their social ties," *PLoS Comput Biol*, vol. 2, p. e140, Oct. 2006.

[114] J. M. Pacheco, A. Traulsen, and M. A. Nowak, "Coevolution of strategy and structure in complex networks with dynamical linking," *Physical Review Letters*, vol. 97, p. 258103, Dec. 2006.

[115] T. Gross, C. J. D. DLima, and B. Blasius, "Epidemic dynamics on an adaptive network," *Physical Review Letters*, vol. 96, p. 208701, May 2006.

[116] D. H. Zanette, "Coevolution of agents and networks in an epidemiological model," *arXiv:0707.1249*, July 2007.

[117] E. Volz and L. A. Meyers, "Susceptibleinfectedrecovered epidemics in dynamic contact networks," *Proceedings of the Royal Society B: Biological Sciences*, vol. 274, pp. 2925–2934, Dec. 2007.

[118] E. Volz and L. A. Meyers, "Epidemic thresholds in dynamic contact networks," *Journal of The Royal Society Interface*, vol. 6, pp. 233–241, Mar. 2009.

[119] S. Van Segbroeck, F. C. Santos, and J. M. Pacheco, "Adaptive contact networks change effective disease infectiousness and dynamics," *PLoS Comput Biol*, vol. 6, no. 8, p. e1000895, 2010.

[120] S. Gil and D. H. Zanette, "Coevolution of agents and networks: Opinion spreading and community disconnection," *Physics Letters A*, vol. 356, pp. 89–94, July 2006.

[121] D. H. Zanette and S. Gil, "Opinion spreading and agent segregation on evolving networks," *Physica D: Nonlinear Phenomena*, vol. 224, pp. 156–165, Dec. 2006.

[122] B. Kozma and A. Barrat, "Consensus formation on adaptive networks," *Physical Review E*, vol. 77, p. 016102, Jan. 2008.

[123] B. Kozma and A. Barrat, “Consensus formation on coevolving networks: groups’ formation and structure,” *Journal of Physics A: Mathematical and Theoretical*, vol. 41, p. 224020, June 2008.

[124] G. Iñiguez, J. Kertész, K. K. Kaski, and R. A. Barrio, “Opinion and community formation in coevolving networks,” *Physical Review E*, vol. 80, p. 066119, Dec. 2009.

[125] A. Galstyan and P. Cohen, “Cascading dynamics in modular networks,” *Physical Review E*, vol. 75, p. 036109, Mar. 2007.

[126] A. De Bruyn and G. L. Lilien, “A multi-stage model of word-of-mouth influence through viral marketing,” *International Journal of Research in Marketing*, vol. 25, pp. 151–163, Sept. 2008.

[127] N. E. Friedkin, “The attitude-behavior linkage in behavioral cascades,” *Social Psychology Quarterly*, vol. 73, pp. 196–213, June 2010.

[128] S. Melnik, J. A. Ward, J. P. Gleeson, and M. A. Porter, “Multi-stage complex contagions,” *Chaos: An Interdisciplinary Journal of Nonlinear Science*, vol. 23, pp. 013124–013124–13, Feb. 2013.

[129] R. Durrett, *Probability: Theory and Examples.* Cambridge University Press, 4 ed., Aug. 2010.

[130] D. Kimura and Y. Hayakawa, “Coevolutionary networks with homophily and heterophily,” *Physical Review E*, vol. 78, July 2008.

[131] F. Vazquez, V. M. Eguíluz, and M. S. Miguel, “Generic absorbing transition in coevolution dynamics,” *Physical Review Letters*, vol. 100, p. 108702, Mar. 2008.

[132] J. L. Herrera, M. G. Cosenza, K. Tucci, and J. C. González-Avella, “General coevolution of topology and dynamics in networks,” *EPL (Europhysics Letters)*, vol. 95, p. 58006, Sept. 2011.

[133] G. A. Böhme and T. Gross, “Analytical calculation of fragmentation transitions in adaptive networks,” *Physical Review E*, vol. 83, p. 035101, Mar. 2011.

[134] R. A. Holley and T. M. Liggett, “Ergodic theorems for weakly interacting infinite systems and the voter model,” *The Annals of Probability*, vol. 3, pp. 643–663, Aug. 1975.

[135] T. M. Liggett, *Stochastic Interacting Systems: Contact, Voter and Exclusion Processes.* Springer, 1999 ed., Nov. 1999.

[136] J. T. Cox and A. Greven, “On the long term behavior of some finite particle systems,” *Probability Theory and Related Fields*, vol. 85, pp. 195–237, June 1990.

[137] C. Borgs, J. Chayes, L. Lovsz, V. Ss, and K. Vesztergombi, “Convergent sequences of dense graphs i: Subgraph frequencies, metric properties and testing,” *Advances in Mathematics*, vol. 219, pp. 1801–1851, Dec. 2008.

[138] G. A. Böhme and T. Gross, “Fragmentation transitions in multistate voter models,” *Physical Review E*, vol. 85, p. 066117, June 2012.